AFRL-AFOSR-UK-TR-2024-0013

Reliable prediction of electronic and optical properties of layered and 2d materials from transferable screened range-separated hybrid functionals

Kronik, Leeor
Weizmann Institute of Science
234 Herzl
REHOVOT, , 00761000
IL

01/02/2024
Final Technical Report

Air Force Research Laboratory
Air Force Office of Scientific Research
European Office of Aerospace Research and Development
Unit 4515 Box 14, APO AE 09421

REPORT DOCUMENTATION PAGE

PLEASE DO NOT RETURN YOUR FORM TO THE ABOVE ORGANIZATION.

1. REPORT DATE	2. REPORT TYPE	3. DATES COVERED	
20240102	Final	START DATE 20200928	END DATE 20230928

4. TITLE AND SUBTITLE
Reliable prediction of electronic and optical properties of layered and 2d materials from transferable screened range-separated hybrid functionals

5a. CONTRACT NUMBER	5b. GRANT NUMBER	5c. PROGRAM ELEMENT NUMBER
	FA8655-20-1-7041	
5d. PROJECT NUMBER	**5e. TASK NUMBER**	**5f. WORK UNIT NUMBER**

6. AUTHOR(S)
Leeor Kronik

7. PERFORMING ORGANIZATION NAME(S) AND ADDRESS(ES)
Weizmann Institute of Science
234 Herzl
REHOVOT 00761000
IL

8. PERFORMING ORGANIZATION REPORT NUMBER

9. SPONSORING/MONITORING AGENCY NAME(S) AND ADDRESS(ES)	10. SPONSOR/MONITOR'S ACRONYM(S)	11. SPONSOR/MONITOR'S REPORT NUMBER(S)
EOARD UNIT 4515 APO AE 09421-4515	AFRL/AFOSR IOE	AFRL-AFOSR-UK-TR-2024-0013

12. DISTRIBUTION/AVAILABILITY STATEMENT
A Distribution Unlimited: PB Public Release

13. SUPPLEMENTARY NOTES

14. ABSTRACT
The accurate description of electronic properties and optical absorption spectra is a longstanding challenge for density functional theory. Recently, the introduction of screened range-separated hybrid (SRSH) functionals for solid-state materials has allowed for the calculation of fundamental band gaps and optical absorption spectra that are in very good agreement with many-body perturbation theory. However, since solid-state SRSH functionals are typically tuned to reproduce the properties of bulk phases, their transferability to low-dimensional structures, which experience substantially different screening than in the bulk, remains an open question. In this project, we explore the transferability of SRSH functionals to several prototypical van der Waals materials, including transition-metal sulfides and selenides, indium selenide, black phosphorus, and hexagonal boron nitride. Considering the bulk and a monolayer of these materials as limiting cases, we show that the parameters of the SRSH functional can be determined systematically, using only the band-edge quasiparticle energies of these extremal structural phases as fitting targets. The resulting SRSH functionals can describe both electronic bandstructures and optical absorption spectra with accuracy comparable to more demanding ab initio many-body perturbation theory (GW and Bethe-Salpeter equation) approaches. Selected examples also demonstrate that the SRSH parameters, obtained from the bulk and monolayer reference structures, display good accuracy for bandstructures and optical spectra of bilayers, indicating a degree of transferability that is independent of the fitting procedure. Moreover, we have applied this methodology to semi-metals, specifically to graphene, proceeding with the fitting to the band gap in a k-point different from the Dirac cone. As a result of the excellent results with the (semi-emprirical) fitting procedure, we have expanded our methodology to a fully non-empirical approach, where the fitting to a band gap in a certain k-point of the Brillouin zone is not needed any longer. For this purpose, we have employed Wannier-localized, optimally tuned, screened range-separated hybrid (WOT-SRSH) functionals, which have been used successfully in the past for determining the electronic band gaps and optical absorption spectra of a variety of molecular and covalent crystals. In this second part of the project, we have developed and applied a fully non-empirical WOT-SRSH approach for determining the functional parameters and we show, using several prototypical vdW materials, that this approach yields a level of accuracy comparable (once more) to that of ab initio many-body perturbation techniques, as the state-of-the-art GW and the Bethe Salpeter equation.

15. SUBJECT TERMS

16. SECURITY CLASSIFICATION OF:			17. LIMITATION OF ABSTRACT	18. NUMBER OF PAGES
a. REPORT	b. ABSTRACT	c. THIS PAGE		
U	U	U	SAR	64

19a. NAME OF RESPONSIBLE PERSON	19b. PHONE NUMBER *(Include area code)*
ANDREW GREENWOOD	314 235 6037

Standard Form 298 (Rev.5/2020)
Prescribed by ANSI Std. Z39.18

AFOSR grant FA8655-20-1-7041

Reliable prediction of electronic and optical properties of layered and 2D materials from transferable screened range-separated hybrid functionals

Final Report

Prof. Leeor Kronik

Sept 1 2020 – Sept 30 2023

Contents

List of Figures

List of Tables

Summary

The accurate description of electronic properties and optical absorption spectra is a long-standing challenge for density functional theory. Recently, the introduction of screened range-separated hybrid (SRSH) functionals for solid-state materials has allowed for the calculation of fundamental band gaps and optical absorption spectra that are in very good agreement with many-body perturbation theory. However, since solid-state SRSH functionals are typically tuned to reproduce the properties of bulk phases, their transferability to low-dimensional structures, which experience substantially different screening than in the bulk, remains an open question. In this project, we explore the transferability of SRSH functionals to several prototypical van der Waals materials, including transition-metal sulfides and selenides, indium selenide, black phosphorus, and hexagonal boron nitride. Considering the bulk and a monolayer of these materials as limiting cases, we show that the parameters of the SRSH functional can be determined systematically, using only the band-edge quasiparticle energies of these extremal structural phases as fitting targets. The resulting SRSH functionals can describe both electronic bandstructures and optical absorption spectra with accuracy comparable to more demanding *ab initio* many-body perturbation theory (GW and Bethe-Salpeter equation) approaches. Selected examples also demonstrate that the SRSH parameters, obtained from the bulk and monolayer reference structures, display good accuracy for bandstructures and optical spectra of bilayers, indicating a degree of transferability that is independent of the fitting procedure. Moreover, we have applied this methodology to semi-metals, specifically to graphene, proceeding with the fitting to the band gap in a k-point different from the Dirac cone. As a result of the excellent results with the (semi-emprirical) fitting procedure, we have expanded our methodology to a fully non-empirical approach, where the fitting to a band gap in a certain k-point of the Brillouin zone is not needed any longer. For this purpose, we have employed Wannier-localized, optimally tuned, screened range-separated hybrid (WOT-SRSH) functionals, which have been used successfully in the past for determining the electronic band gaps and optical absorption spectra of a variety of molecular and covalent crystals. In this second part of the project, we have developed and applied a fully non-empirical WOT-SRSH approach for determining the functional parameters and we show, using several prototypical vdW materials, that this approach yields a level of accuracy comparable (once more) to that of *ab initio* many-body perturbation techniques, as the state-of-the-art GW and the Bethe Salpeter equation.

1 Introduction

The determination of the many-body properties of materials, such as the electronic band structure, is crucial to the have precise knowledge of their transport and optical properties [1]. Charge transport is determined by the range of energies that an electron can have in a periodic solid, which is provided by its band structure. Optical properties that arise after absorption of a photon by an electron (the electron being promoted to a higher energy level and leaving a hole behind) require the introduction of a new quasi-particle called exciton, which results from the interaction and binding of the excited electron-hole pair.

Nowadays, *state of the art* first-principles materials research mostly employs many-body perturbation theory (MBPT) to find the electronic and optical properties with high accuracy. Specifically, one typically uses a combination of the GW approximation (to obtain the correct bandstructure) and the Bethe-Salpeter equation (BSE) [2]–[4] to compute optical spectra and excitonic properties. This combination of techniques provides proper electronic correlation effects and Coulomb screening that are missing in other standard approaches to solve the electronic structure problem, such as standard density functional theory (DFT) [5], [6]. However, GW-BSE is computationally expensive [4], [7]–[9] and there is ongoing interest in developing alternative approaches that can provide results with similar accuracy at a lower computational cost.

A first-principles alternative to MBPT is density functional theory [5], [6], as well as its extension to the time-domain, namely time-dependent DFT (TDDFT) [10], [11]. However, it is well known that (TD)DFT with common approximate functionals often fails in the prediction of electronic and optical excitations in solids [2]. One promising recent approach within DFT is that of the tuned screened range-separated hybrid functional (SRSH) [12], [13]. This is important, because although the formal scaling of GW and of DFT with a hybrid functional is the same, in practice the latter can be markedly faster and requires substantially less memory [14], [15], primarily owing to the lack of explicit construction of the dielectric matrix. The latter is specially important in materials where screening plays a fundamental role.

In the SRSH approach, the Coulomb potential is split into short and long range components [16], [17]. In the long range, we ensure the asymptotic behaviour that Hartree-Fock theory provides, while in the short range we mimic the behavior of a standard hybrid functional [18]. A range separation parameter, which dictates the range at which one gradually crosses over from short-range to long-range behavior, can be chosen, for instance, by imposing the ionization potential theorem [19]–[22]. Although these functionals were originally developed for molecular systems [23], [24], they have recently been employed to obtain reliable predictions of the electronic structure and optical spectra of solids, sometimes even surpassing the accuracy of GW-BSE for periodic systems, such as in molecular solids [25], [26] and bulk semiconductors and insulators [27]–[29]. Calculations using SRSH functionals and time-dependent DFT (TDDFT) have been also successfully benchmarked against standard GW-BSE calculations when spin-orbit coupling is relevant [28]–[31].

An important family of materials are van der Waals (vdW) layered materials, which have been in the spotlight for almost two decades [32]–[34], also attracting an enormous amount of attention since the experimental isolation of graphene in 2004 [35], [36]. These materials present an inherently wide range of structural, electronic, and optical properties, which is vastly enhanced by the possibility of combining layers (e.g., through

heterostructuring, as well as relative twisting or sliding) to allow for additional tuning of their physicochemical properties.[32]–[34], [37]–[43]. As the space of vdW materials and their derivatives continues to expand, there is an ever growing need for a reliable theoretical description of their electronic and optical properties, particularly bandstructures and optical absorption spectra.

As highlighted above, state-of-the-art first-principles calculations of these properties in vdW materials are based mostly on MBPT [2], [44]. *Ab initio* MBPT is usually employed in practice by using the GW approximation [45] with input from a (generalized) Kohn-Sham eigensystem to obtain single quasi-particle excitation energies and the Bethe-Salpeter equation (BSE) [46], [47] to calculate neutral excitation energies and optical absorption spectra. Indeed, GW-BSE has been found to be very successful in the interpretation and even prediction of electronic and optical properties in vdW materials (e.g., refs [48]–[53]). However, GW-BSE calculations are relatively expensive computationally [4], [54], [55], and specifically can become prohibitively expensive especially when supercells are called for, e.g. in the calculation of defects or of twisted multilayer structures. Therefore, there remains a need for alternative computational approaches that can provide results with similar accuracy at a substantially lower computational cost.

In our AFOSR-sponsored research, we focus on the application of screened ranged-separated (SRSH) functionals to two-dimensional and layered materials [56]. In our preliminary work on the topic, we reported promising results on the transferability between different two-dimensional and bulk phases of MoS_2 and hexagonal boron nitride (h-BN). We showed that an accurate prediction of the band structure over the entire Brillouin zone for MoS_2 and h-BN, as compared to GW calculations, is obtained by fitting the SRSH α and γ parameters to only one quasiparticle energy. However, when optical absorption spectra are calculated using time-dependent (TD-)SRSH, we observe discrepancies. Although the agreement with the GW-BSE calculations is excellent for MoS_2, deviations are observed in the case of h-BN. These results led to several questions and objectives that we explore within the scope of this project:

1. Benchmarking of two-dimensional and layered van der Waals materials that present a large variation in the energy band gap (from large band gap, e.g. hexagonal-boron nitride (h-BN), to gapless materials, e.g. graphene).

2. Two-dimensional systems are highly anisotropic. Is this approach valid for an anisotropic dielectric response? What are the limitations of this approach?

3. Is the use of a single dielectric constant enough to get reliable and accurate results for electronic and optical properties? Which circumstances allow the use of such approximation? Can we develop an empirical model which captures the anisotropy of the dielectric response in two-dimensional systems? Does this new empirical model improve the results?

4. If the previous points are successful, can we benchmark more complex structures? For example, heterostructures composed of layers of different materials, or layers with defects?

5. Can we extend the methodology of the SRSH functionals from a semi-empirical approach to a fully non-empirical method?

The answer to these questions are treated in this report. Part of the results within have been published in María Camarasa-Gómez, Ashwin Ramasubramaniam, Jeffrey B. Neaton, and Leeor Kronik, 'Transferable screened range-separated hybrid functionals for electronic and optical properties of van der Waals materials', Phys. Rev. Materials 7, 104001 (2023), and part of the results shown will be showed in the publication under preparation, and that we aim at submitting soon, with the working title 'Fully Non-Empirical Determination of Electronic and Optical Properties of van der Waals Materials from a Wannier-localized Optimally Tuned Screened Range-Separated Hybrid Functional', to be authored by María Camarasa-Gómez, Stephen E. Gant, Guy Ohad, Ashwin Ramasubramaniam, Jeffrey B. Neaton, and Leeor Kronik.

2 Methods, Assumptions, and Procedures

2.1 Theory of the SRSH Functional

In the SRSH approach, the Coulomb operator is partitioned into short range (SR) and long range (LR) components through the introduction of three parameters, α, β, γ, as follows [16], [17]:

$$\frac{1}{r} = \frac{\alpha + \beta\,\mathrm{erf}(\gamma r)}{r} + \frac{1 - [\alpha + \beta\,\mathrm{erf}(\gamma r)]}{r}, \tag{1}$$

where $\mathrm{erf}(\cdot)$ is the error function, r is the inter-electron distance, and γ is a range-separation parameter. The first term of Eq. (1) is treated using exact exchange while the second term is treated using a semilocal approximation. The parameter α therefore sets the fraction of exact exchange in the short range, the sum of parameters $\alpha + \beta$ sets the fraction of exact exchange in the long range, and $1/\gamma$ provides a length-scale for the crossover from short- to long-range behavior, interpolated smoothly by the error function [18]. To enforce a correct asymptotic behaviour of the screened Coulomb operator via appropriate dielectric screening, we impose the condition $\alpha + \beta = 1/\epsilon_\infty$, where ϵ_∞ is the high-frequency scalar (orientationally-averaged) dielectric constant [25]. Enforcing this limit is essential to capturing excitonic effects in solid-state systems [25], [30], [57]. The above relation fixes the value of β, given a choice of α, in terms of ϵ_∞, leaving two free parameters: α and γ. This approach neglects anisotropy and approximates the dielectric constant as a scalar, i.e., $\epsilon_\infty = \mathrm{Tr}[\boldsymbol{\epsilon}_\infty]/3$. For 2D systems, we set $\epsilon_\infty = 1$, which is the correct asymptotic limit of screening in the long range for an isolated 2D system [58], [59].

With these ingredients at hand, the exchange potential of the SRSH functional, derived within generalized Kohn-Sham theory [24], [60]–[62], is represented by the non-multiplicative potential operator

$$v_x^{\mathrm{SRSH}} = \alpha v_{\mathrm{XX}}^{\mathrm{SR}} + (1-\alpha) v_{\mathrm{SL}}^{\mathrm{SR}} + \frac{1}{\epsilon_\infty} v_{\mathrm{XX}}^{\mathrm{LR}} + \left(1 - \frac{1}{\epsilon_\infty}\right) v_{\mathrm{SL}}^{\mathrm{LR}}, \tag{2}$$

where the subscripts 'x', 'XX', and 'SL' denote exchange, exact (Fock) exchange, and semi-local exchange, respectively.

2.2 Methodology

In this project, we expand two different approaches, already tested in Refs. [56] (semi-empirical approach) and [27] (fully non-empirical approach) to obtain the parameters α, γ, and ϵ_∞ that uniquely determine the SRSH functional for a given material. The semi-empirical approach is the first approximation to the determination of the SRSH parameters. The fully non-empirical approach appears as a result of the successful results obtained with the first one, as seen in Sec. 3.1. A key feature of SRSH functionals is the proper incorporation of dielectric screening in the long-range exchange, which assures the correct asymptotic decay of the Coulomb tail [12], [13], [16], [17], [25]. However, in vdW materials the dielectric constant varies with the number of layers between its bulk value and unity – formally, the correct asymptotic limit for screening in a monolayer [58], [59] – introducing a potentially large structure dependence to the parameters of the SRSH functional. Therefore, an open question remains as to whether an SRSH functional that

is optimally tuned, say, for the bulk phase of a material, would be transferable to lower-dimensional structures. We compute the scalar dielectric constant, ϵ_∞, for bulk phases, which is determined non-empirically using the random phase approximation [63] (RPA) that includes local-field effects at the Hartree level of a (semi-)local functional. Other approaches are equally valid, but we choose to use the RPA to maintain consistency between the treatment of the dielectric response in the DFT and the GW calculations. The calculated values of ϵ_∞ for the bulk phases of various materials studied here are listed in Table 3. For monolayers and bilayers, we use a value of $\epsilon_\infty = 1$, as discussed above.

In the semi-empirical approach (see the sketch of the method in Figure 1), to determine suitable values of α and γ for each material, we perform GW calculations to determine the quasiparticle gaps for the bulk and monolayer structures. For monolayers, these quasiparticle gaps are extrapolated to the limit of infinite vacuum. We then perform a sweep over the $\alpha - \gamma$ parameter space and calculate the corresponding SRSH band gaps for pairs of values (α, γ). We quantify the error in the SRSH calculation, relative to the reference GW result, by the difference between the quasiparticle and SRSH band gaps at a particular k-point, $\Delta E_\mathrm{g} = E_g^\mathrm{GW} - E_g^\mathrm{SRSH}$. We find that it is generally sufficient to ensure that $\Delta E_\mathrm{g} = 0$ at just one high-symmetry k-point, which we pick to correspond to the smallest direct band gap.

As noted in prior work [30], [56], [64], [65], the choice of α and γ is not unique for a particular material (or phase) and the tuning procedure outlined above generally leads to a continuum of values that lie on a "zero-crossing" line, $\Delta E_\mathrm{g} = 0$, of the $\Delta E_\mathrm{g}(\alpha, \gamma)$ surface. Given two phases – the bulk and monolayer – the intersection of their individual zero-crossing lines leads to a unique set of parameters, (α^*, γ^*), that is simultaneously optimal for both phases. It is this optimal pair that is finally used for computing electronic and optical properties of the various materials.

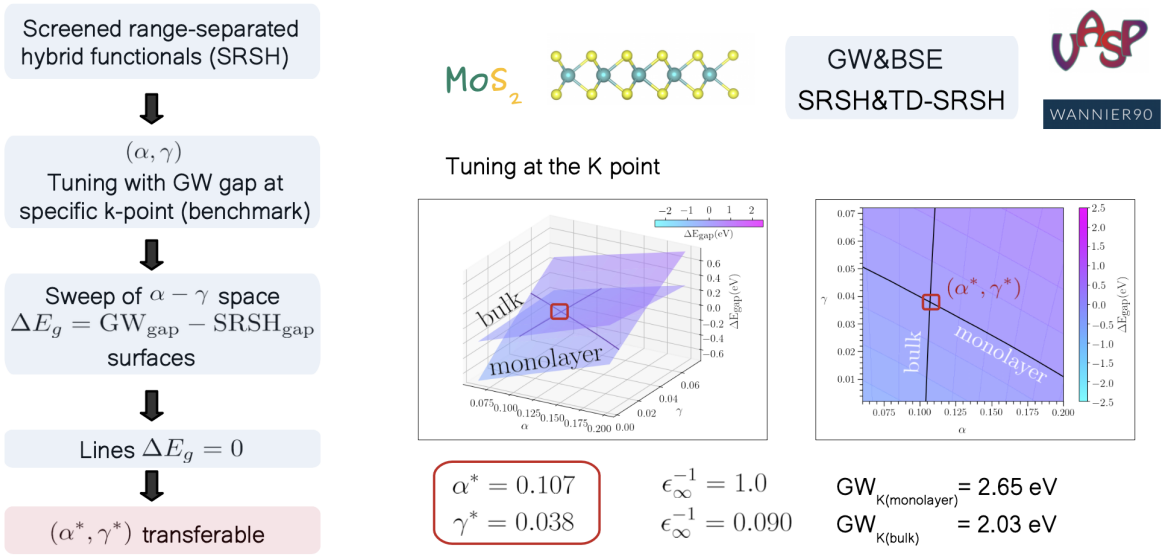

Figure 1: Sketch of the procedure for the semiempirical approach for Mo_2 at the K point of the Brillouin zone once the dielectric constant for the bulk system is calculated within the RPA approximation. This method was firstly tested in Ref. [56]. On the left part we specify the steps taken to obtained the results shown on the right part. The electronic structure calculations were done using VASP and the band structures were obtained using the Wannier90 code. The benchmark calculations were done employing G_0W_0-BSE method. In the lower right part the inverse dielectric function as well as the G_0W_0@LDA band gap at the K point are indicated. The numbers in the red square are the transferable parameters for the SRSH found following the semiempirical procedure.

In the fully non-empirical approach, the procedure of selecting γ is often carried out by enforcing an exact physical condition, the ionization potential theorem (IPT) [19]–[22] (see Fig. 2). This method, known as optimal tuning, has shown great success in the prediction of fundamental gaps of molecules [23], [24], [66]–[71]. In the bulk limit, however, optimal tuning fails because the IPT is trivially satisfied for every parametrization of SRSH (or indeed any functional) [72]–[75], such that the uniqueness of the optimally tuned γ that is achieved in molecules is lost.

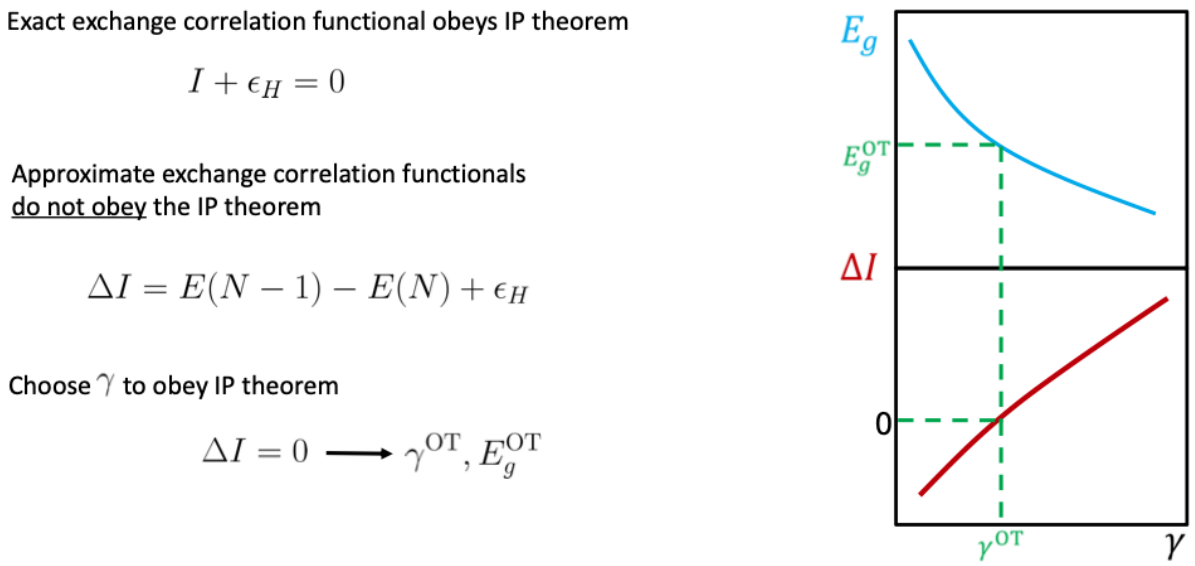

Figure 2: Sketch of the application of the IP theorem to get the optimal value for the γ parameter.

The reason for the failure of optimal tuning in the bulk limit is the natural delocalization of the electronic orbitals (see Figure 3). Recently, a number of studies have exploited different localization schemes for electronic structure predictions [76]–[92]. Similarly, the WOT-SRSH approach adopts a criterion that generalizes the IPT to the removal of charge from a maximally localized Wannier function [27]. This *ansatz*, inspired by Ma and Wang [77], is given by

$$\Delta I^{\gamma} = E^{\gamma}_{\mathrm{constr}}[\phi](N-1) - E^{\gamma}(N) + \langle\phi|\, \hat{H}^{\gamma}_{\mathrm{SRSH}}\, |\phi\rangle = 0, \tag{3}$$

where $E^{\gamma}(N)$ is the total energy of the system with N electrons and $E^{\gamma}_{\mathrm{constr}}[\phi](N-1)$ is the total energy of a system with one electron removed from a Wannier function ϕ, including an image charge correction (see Refs. [27]–[29] for further details). $\langle\phi|\, \hat{H}^{\gamma}_{\mathrm{SRSH}}\, |\phi\rangle$ is the expectation value for the energy of the Wannier function with respect to the SRSH Hamiltonian of an N electron system. The energy of the charged system is calculated under a constraint that allows one to control the occupation of the Wannier function via the Lagrange multiplier λ [27]. The constraint is imposed using the equation

$$\hat{H}_{\mathrm{SRSH}}\, |\psi_i\rangle + \lambda\, |\phi\rangle\, \langle\phi|\psi_i\rangle = \epsilon_i\, |\psi_i\rangle\,, \tag{4}$$

where $\{\psi_i\}$ and $\{\epsilon_i\}$ are the GKS eigenfunctions and eigenvalues, respectively, of the constrained $(N-1)$-electron system.

Here, the WOT-SRSH procedure is carried out in an iterative manner, based and adapted from the scheme suggested by Wing *et al.* [27]. In step 1, the dielectric constant, ε_∞, is calculated in the primitive unit cell within the RPA approximation. In step 2,

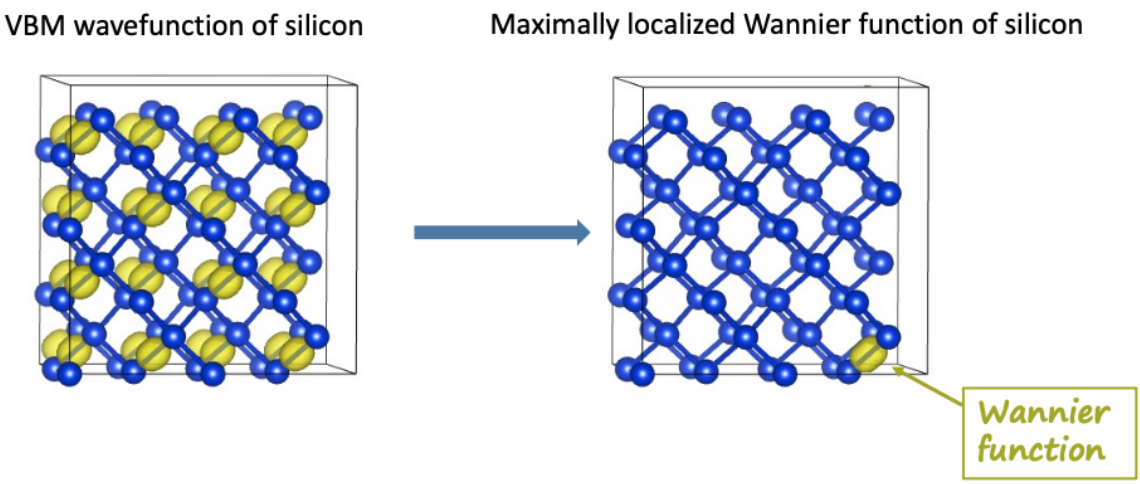

Figure 3: Example of the localization of a Wannier function in a silicon supercell. On the left, the delocalized orbital corresponding to the valence band maximum of silicon. On the right the maximally localized Wannier function with the highest energy of the valence bands.

we compose maximally localized Wannier functions from the topmost valence bands in a supercell. We then select the Wannier function with highest energy in the manifold and use it in step 3, where we enforce the *ansatz* given in Eq. (3) by selecting the range-separation parameter γ so that $\Delta I^{\gamma} = 0$ for the supercell and for different values of α. In step 4 we calculate the crossings of α and γ that fulfill the IP ansatz for both the bulk and the monolayer phases. Finally, in step 5 we calculate properties of interest with the selected α and γ. This method is summarized in Figure 4. We also apply a model for the image-charge correction as similarly done in Ref. [27]–[29] and we incorporate the fact that the monolayer vdW supercells have a vacuum layer by a correction of the z-component of the dielectric tensor based on Ref. [93]. The reason is that in the supercell calculations for the vdW monolayer the approximation $\epsilon_{\infty} = 1.0$ only holds for the x- and y-directions. Essentially we consider a model of capacitors, where the x- and y-components will remain the same as in the bulk dielectric tensor, and we will apply the model to the z-component.

Using these two procedures, we determine transferable pairs, (α^*, γ^*), for various vdW materials and compare their electronic bandstructures against those obtained from GW calculations. We also report optical absorption spectra obtained from linear response [94] TD-SRSH calculations [12], [26], [30], and compare the results against GW-BSE calculations within the Tamm-Dancoff approximation [95].

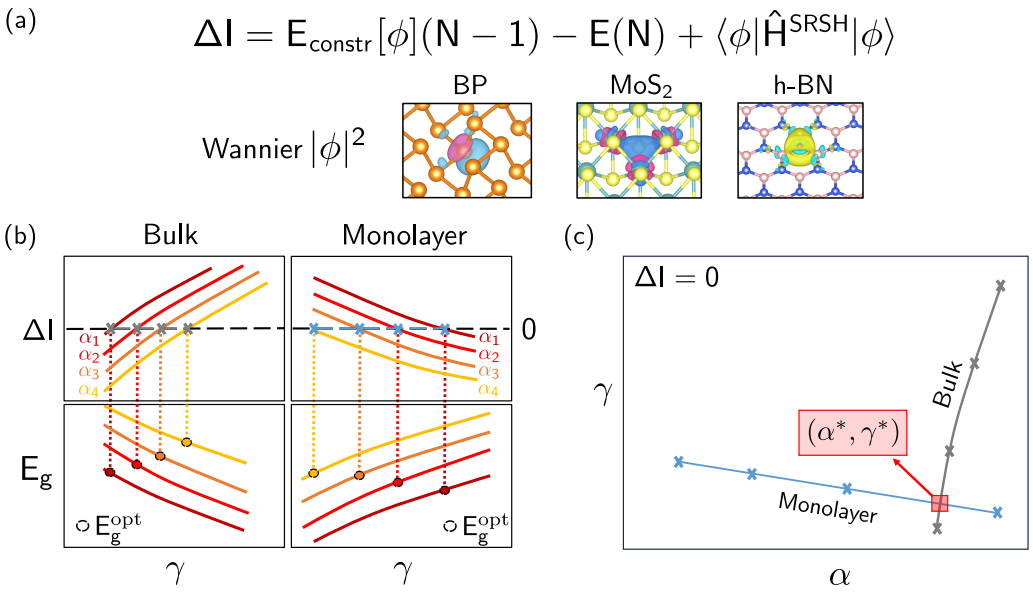

Figure 4: Sketch of the WOT-SRSh method for vdW materials. employed for the removal of the semi-empirical approach for the SRSH functionals for vdW materials. Panel (a) shows the *ansatz* followed in the procedure of WOT-SRSH ([27]), as well as examples of maximally localized Wannier functions for each of the materialas where the fully non-empirical approach has been used. (b) The upper plots represent the application of the *ansatz* for different values of the exchange α. In the lower plots we show the flow of the band gap value as an outcome of the applucation of the *ansatz*. Panel (c) represents the transferability between the monolayer and bulk when the two curves cross in the $\Delta I = 0$ plane of the $\alpha - \gamma$ space.

2.3 Computational details

We have performed the (TD-)SRSH and the GW(-BSE) calculations using a modified home version of the *Vienna Ab initio Simulation Package* [96], [97] (VASP). We have obtained the band structures, for both GW and SRSH calculations, with *Wannier90*. We have performed the analysis of the data with home-made scripts using Python 3.

The GW flavor of the projector-augmented-wave pseudopotentials [98], [99] (PAW) provided by VASP have been employed throughout, in both DFT and GW calculations. LDA-based PAWs were used for molybdenum disulfide (MoS_2) and hexagonal-boron nitride (h-BN), using an energy cutoff of 500 eV and 550 eV, respectively. PBE-based PAWs were used for the rest of the materials, employing energy cutoffs for the monolayer and the bulk phases, respectively, of 450 and 600 eV for molybdenum diselenide ($MoSe_2$), 600 eV for tungsten diselenide (WSe_2), 550 and 600 eV for tungsten disulfide (WS_2), 500 and 550 eV for indium selenide (InSe), and 400 and 450 eV for black phosphorus (BP). The electronic configuration for the valence electrons are $4s^2 4p^6 5s^1 4d^5$ for Mo, $3s^2 3p^4$ for S, $2s^2 2p^1$ for B, $2s^2 2p^3$ for N, $5p^6 6s^2 5d^4$ for W, $4s^2 4p^4$ for Se, $5s^2 5p^1$ for In, and $3s^2 3p^3$ for P.

The (semi-)local exchange-correlation used as ingredients in the SRSH calculations, as well as in the preparation of the wavefunctions employed in the GW calculations, has been the local density approximation [100], [101] (LDA) for MoS_2 and h-BN. For BP, GW calculations were performed based on a DFT starting point calculated with the Heyd-Scuseria-Ernzerhof[102], [103] (HSE) functional, and the Perdew-Burke-Ernzerhof[104] (PBE) approximation for the rest of materials presented in this work.

Benchmarks for the band structures and optical absorption spectra of the (time-dependent) screened range-separated hybrid functionals (TD-SRSH) are performed in a

similar fashion to that reported in Ref. [56], employing the one-shot flavour of GW and the Bethe-Salpeter equation (BSE)[2]–[4]. Given the lack of Coulomb cutoff correction in VASP, the extrapolation of the band gap obtained with the G_0W_0 benchmarks to an infinite vacuum distance is needed, and we report the selection of the band gap in Sec. 3.1.1. The macroscopic dielectric constants for the bulk systems were obtained for all materials using the Random Phase Approximation [63] (RPA) based on PBE, except for the case of BP, where it was calculated using the HSE functional. Spin-orbit coupling (SOC) has been taken into account only in TD-SRSH optical absorption spectra of monolayers for WS_2, WSe_2, $MoSe_2$, InSe monolayers, and the MoS_2 bilayer. All band structures were obtained through Wannier interpolation using Wannier90 [105].

All atomic structures employed in this work are given in Sec. 2.4 and were not relaxed. Only the bulk phase of BP was fully relaxed, with residual forces smaller than 0.01 eV/Å, with an energy tolerance smaller than 10^{-8} eV, and using Tkatchenko-Scheffler dispersion corrections [106].

We also calculated in the fully non-empirical approach the zero-point renormalization band gap for hexagonal boron nitride employing BerkleyGW.

2.4 Atomic Geometries

In this section, we provide the atomic structures of the bulk and monolayers employed in all the calculations of the project in the format of VASP. The monolayer structures are obtained from the bulk by isolating a single layer and adding vacuum in the direction perpendicular to the plane of the monolayer.

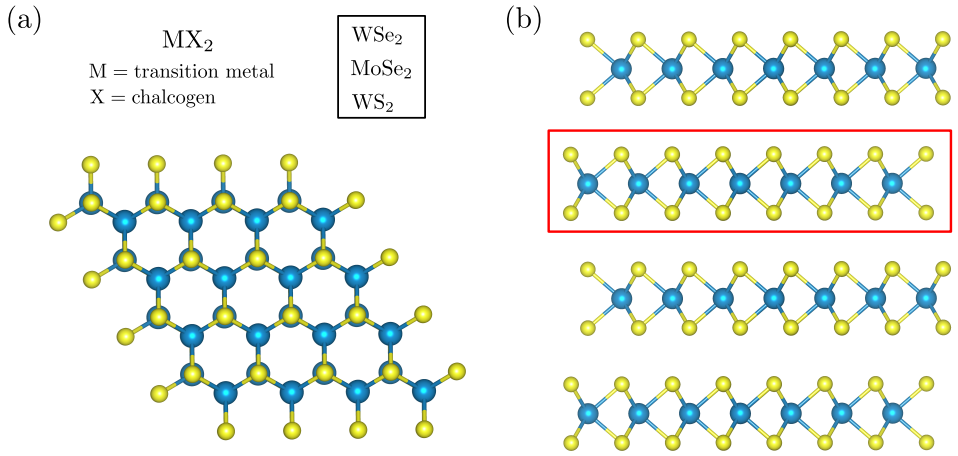

Figure 5: Atomic structure for WS_2: (a) Top view and general chemical formula for transition metal dichalcogenides, and (b) lateral view. The red square contains the monolayer structure. WSe_2 and $MoSe_2$ present a similar structure.

Unit cell of WS_2: Atomic structure obtained from Ref. [107].

Bulk WS_2
W S2
1.0
3.1531999111 0.0000000000 0.0000000000
-1.5765999556 2.7307512262 0.0000000000
0.0000000000 0.0000000000 12.3229999542
W S
2 4
Cartesian
0.000000000 1.820500872 3.080749989
1.576599862 0.910250354 9.242249966
0.000000000 1.820500872 7.671067501
1.576599862 0.910250354 4.651932453
1.576599862 0.910250354 1.509567524
0.000000000 1.820500872 10.813432430

Monolayer WS_2
W S2
1.0
3.1531999111 0.0000000000 0.0000000000
-1.5765999556 2.7307512262 0.0000000000
0.0000000000 0.0000000000 20.0
W S
1 2
Cartesian
0.000000000 1.820500872 3.080749989
1.576599862 0.910250354 4.651932453
1.576599862 0.910250354 1.509567524

In the basis of the reciprocal lattice vectors, the coordinates of the high-symmetry **k**-points in the Brillouin zone are:
$\Gamma = (0.0, 0.0, 0.0)$,
$\mathrm{K} = (1/3, 1/3, 0.0)$,
$\mathrm{M} = (1/2, 0.0, 0.0)$.

Unit cell of WSe_2 Atomic structure obtained from Ref. [107].

Bulk WSe_2
W Se2
1.0
3.2820000648 0.0000000000 0.0000000000
-1.6410000324 2.8422954314 0.0000000000
0.0000000000 0.0000000000 12.9600000381
W Se
2 4
Cartesian
0.000000000 1.894863677 3.240000010
1.640999935 0.947431754 9.720000029
0.000000000 1.894863677 8.049456134
1.640999935 0.947431754 4.910543904
1.640999935 0.947431754 1.569456115
0.000000000 1.894863677 11.390543924

Monolayer WSe_2
W Se2
1.0
3.2820000648 0.0000000000 0.0000000000
-1.6410000324 2.8422954314 0.0000000000
0.0000000000 0.0000000000 20.0
W Se
1 2
Cartesian
0.000000000 1.894863677 3.240000010
1.640999935 0.947431754 4.910543904
1.640999935 0.947431754 1.569456115

In the basis of the reciprocal lattice vectors, the coordinates of the high-symmetry **k**-points in the Brillouin zone are:
$\Gamma = (0.0, 0.0, 0.0)$,
$\mathrm{K} = (1/3, 1/3, 0.0)$,
$\mathrm{M} = (1/2, 0.0, 0.0)$.

Unit cell for $MoSe_2$

Atomic structure obtained from Ref. [108].

Bulk $MoSe_2$

Mo Se2
1.0
3.2850000858 0.0000000000 0.0000000000
-1.6425000429 2.8448935258 0.0000000000
0.0000000000 0.0000000000 12.9010000229
Mo Se
2 4
Cartesian
0.000000000 1.896595740 3.225250006
1.642499945 0.948297785 9.675750017
0.000000000 1.896595740 8.063125014
1.642499945 0.948297785 4.837875009
1.642499945 0.948297785 1.612625003
0.000000000 1.896595740 11.288375020

Monolayer $MoSe_2$

Mo Se2
1.0
3.2850000858 0.0000000000 0.0000000000
-1.6425000429 2.8448935258 0.0000000000
0.0000000000 0.0000000000 20.0
Mo Se
1 2
Cartesian
0.000000000 1.896595740 3.225250006
1.642499945 0.948297785 4.837875009
1.642499945 0.948297785 1.612625003

In the basis of the reciprocal lattice vectors, the coordinates of the high-symmetry **k**-points in the Brillouin zone are:
$\Gamma = (0.0, 0.0, 0.0)$,
$\mathrm{K} = (1/3, 1/3, 0.0)$,
$\mathrm{M} = (1/2, 0.0, 0.0)$.

Unit cell of black phosphorus

The atomic structure was obtained from Ref. [109]. Note that for this material alone, the bulk structure was relaxed, as noted before. The monolayer was then derived from the bulk structure without further structural relaxation.

Bulk black phosphorus

P
1.0
3.3132998943 0.0000000000 0.0000000000
0.0000000000 10.4729995728 0.0000000000
0.0000000000 0.0000000000 4.3740000725
P
8
Cartesian
0.000000000 1.082908150 0.352544410
0.000000000 9.390091501 4.021455565
0.000000000 4.153591714 2.539544544
0.000000000 6.319407858 1.834455659
1.656649947 6.319407858 0.352544410
1.656649947 4.153591714 4.021455565
1.656649947 9.390091501 2.539544544
1.656649947 1.082908150 1.834455659

Monolayer black phosphorus

P
1.0
3.3149049282 0.0000000000 0.0000000000
0.0000000000 4.4248895645 0.0000000000
0.0000000000 0.0000000000 20.0
P
4
Cartesian
0.000000000 2.575827533 2.143897536
0.000000000 1.849062296 0.000000000
1.657452464 0.363382520 0.000000000
1.657452464 4.061507078 2.143897536

In the basis of the reciprocal lattice vectors, the coordinates of the high-symmetry **k**-points in the Brillouin zone are:
$\Gamma = (0.0, 0.0, 0.0)$,
$\mathrm{X} = (1/2, 0.0, 0.0)$,
$\mathrm{S} = (1/2, 1/2, 0.0)$,
$\mathrm{Y} = (0.0, 1/2, 0.0)$.

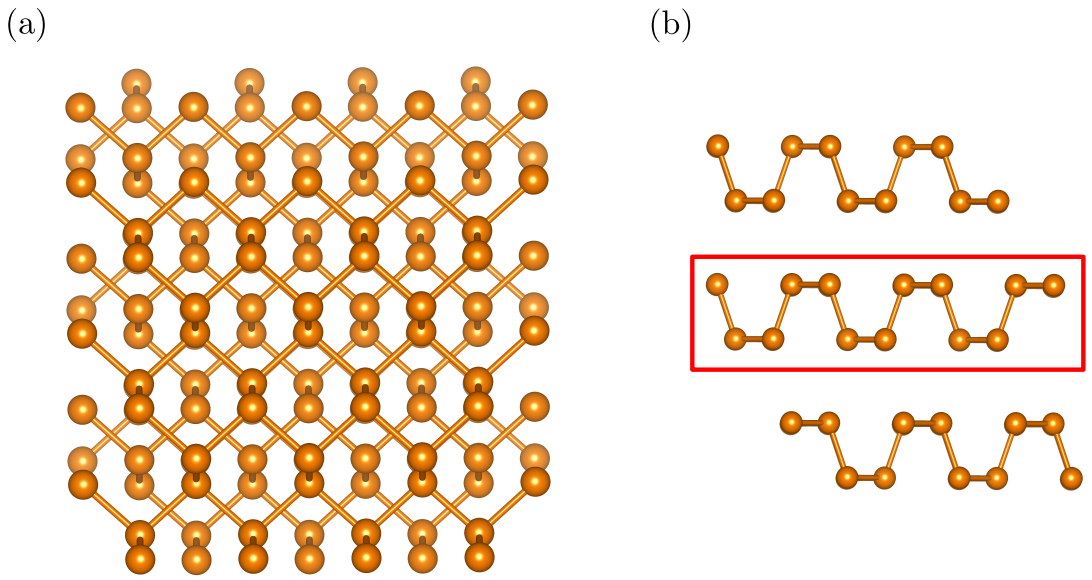

Figure 6: Atomic structure for black phosphorus (BP): (a) Top view, and (b) lateral view. The red square contains the monolayer structure.

Unit cell of InSe

The atomic structure was obtained from Ref. [110].

Bulk InSe

In Se
1.0
4.0036997795 0.0000000000 0.0000000000
-2.0018498898 3.4673057182 0.0000000000
0.0000000000 0.0000000000 16.6439990997
In Se
4 4
Cartesian
0.000000000 2.311537214 2.794527383
2.001849770 1.155768504 13.849472213
2.001849770 1.155768504 11.116526437
0.000000000 2.311537214 5.527472167
0.000000000 2.311537214 15.146038625
2.001849770 1.155768504 1.497959978
2.001849770 1.155768504 6.824039571
0.000000000 2.311537214 9.819960024

Monolayer InSe

In Se
1.0
4.0036997795 0.0000000000 0.0000000000
-2.0018498898 3.4673057182 0.0000000000
0.0000000000 0.0000000000 20.0
In Se
2 2
Cartesian
0.000000000 2.311537214 2.794527383
0.000000000 2.311537214 5.527472167
2.001849770 1.155768504 1.497959978
2.001849770 1.155768504 6.824039571

In the basis of the reciprocal lattice vectors, the coordinates of the high-symmetry **k**-points in the Brillouin zone are:
$\Gamma = (0.0, 0.0, 0.0)$,
$\mathrm{K} = (1/3, 1/3, 0.0)$,
$\mathrm{S} = (1/2, 0.0, 0.0)$.

Bilayer MoS_2

The atomic structure was obtained from Ref. [111].

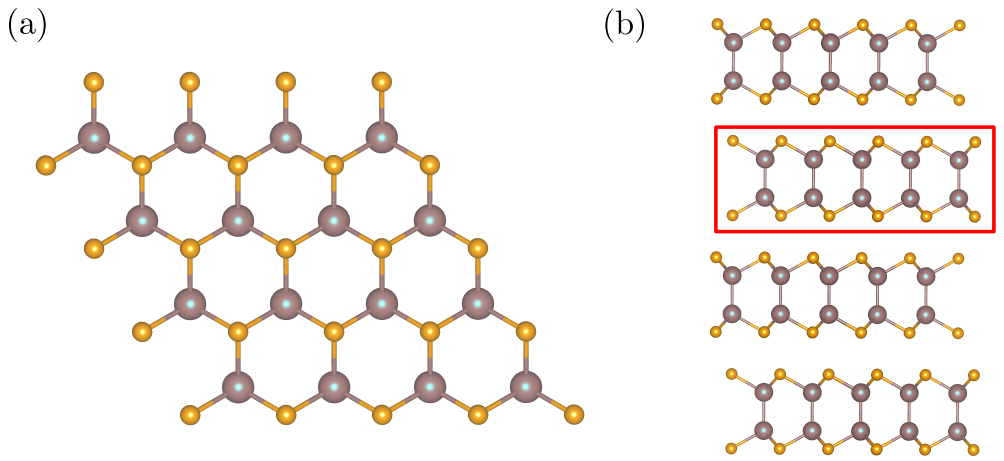

Figure 7: Atomic structure for InSe: (a) Top view, and (b) lateral view. The red square contains the monolayer structure.

Mo S2
1.0
3.1610000134 0.0000000000 0.0000000000
-1.5805000067 2.7375063129 0.0000000000
0.0000000000 0.0000000000 28.0
Mo S
2 4
Cartesian
0.000000000 1.825004263 3.073750019
1.580499912 0.912502050 9.221250057
0.000000000 1.825004263 7.715112519
1.580499912 0.912502050 4.579887558
1.580499912 0.912502050 1.567612480
0.000000000 1.825004263 10.727387596

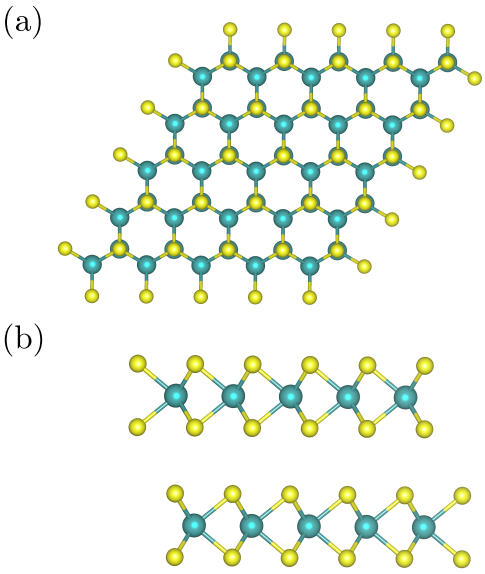

Figure 8: Atomic structure for bilayer MoS_2: (a) Top view, and (b) lateral view.

In the basis of the reciprocal lattice vectors, the coordinates of the high-symmetry **k**-points in the Brillouin zone are:
$\Gamma = (0.0, 0.0, 0.0)$,
$\mathrm{K} = (1/3, 1/3, 0.0)$,
$\mathrm{M} = (1/2, 0.0, 0.0)$.
These coordinates also apply to the high-symmetry points of the monolayer and bulk band structures shown in this report.

Bilayer h-BN

The atomic structure was obtained from Ref. [112].

BN
1.0
2.4982399940 0.0000000000 0.0000000000
-1.2491199970 2.1635392996 0.0000000000
0.0000000000 0.0000000000 23.0
B N
2 2
Cartesian
0.000000000 0.000000000 3.317850113
0.000000000 1.442359576 0.000000000
0.000000000 0.000000000 0.000000000
0.000000000 1.442359576 3.31785011

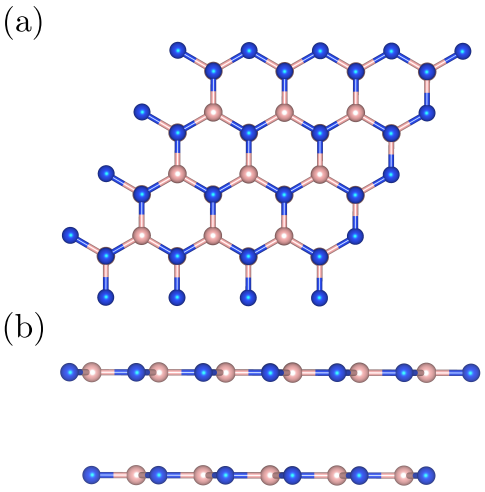

Figure 9: Atomic structure for bilayer h-BN: (a) Top view, and (b) lateral view.

In the basis of the reciprocal lattice vectors, the coordinates of the high-symmetry **k**-points in the Brillouin zone are:
$\Gamma = (0.0, 0.0, 0.0)$,
$\mathrm{K} = (1/3, 1/3, 0.0)$,
$\mathrm{M} = (1/2, 0.0, 0.0)$.
These coordinates also apply to the high-symmetry points of the monolayer and bulk band structures shown in this report.

Graphene

The atomic structure was obtained from Ref. [113].

C
1.0
2.4560000896 0.0000000000 0.0000000000
-1.2280000448 2.1269584693 0.0000000000
0.0000000000 0.0000000000 26
C
2
Cartesian
0.000000000 0.000000000 0.000000000
0.000000000 1.417972355 0.000000000

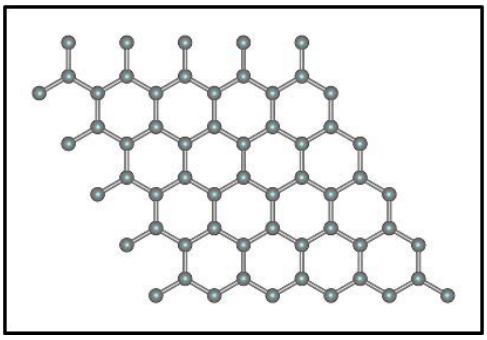

Figure 10: Atomic structure for graphene (top view).

Graphite

C
1.0
2.4560000896 0.0000000000 0.0000000000
-1.2280000448 2.1269584693 0.0000000000
0.0000000000 0.0000000000 6.6960000992
C
4
Cartesian
0.000000000 0.000000000 0.000000000
0.000000000 0.000000000 3.348000050
0.000000000 1.417972355 0.000000000
1.227999972 0.708986114 3.348000050

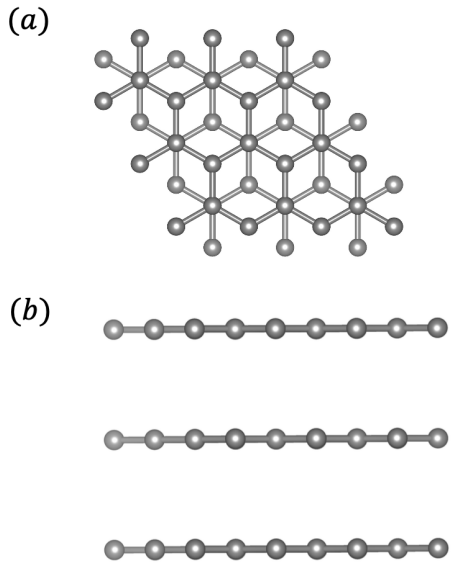

Figure 11: Atomic structure for graphite, (a) top view and (b) lateral view.

In the basis of the reciprocal lattice vectors, the coordinates of the high-symmetry **k**-points in the Brillouin zone are:
$\Gamma = (0.0, 0.0, 0.0)$,
$\mathrm{K} = (1/3, 1/3, 0.0)$,
$\mathrm{M} = (1/2, 0.0, 0.0)$.
These coordinates also apply to the high-symmetry points of the monolayer and bulk band structures shown in this report.

3 Results and Discussion

3.1 Semi-empirical fitting approach

In this section, we apply the methodology described in Section 2.2 corresponding to the semi-emprical fitting approach to representative vdW materials: these include transition-metal dichalcogenides (TMDCs) WS_2, WSe_2 and $MoSe_2$; black phosphorus (BP); and InSe. These materials range from narrow- to medium-gap semiconductors.

3.1.1 Convergence of G_0W_0 Calculations

In this section we provide the extrapolation of the quasiparticle bandgaps and the selected bandgap fitting target for the SRSH calculations.

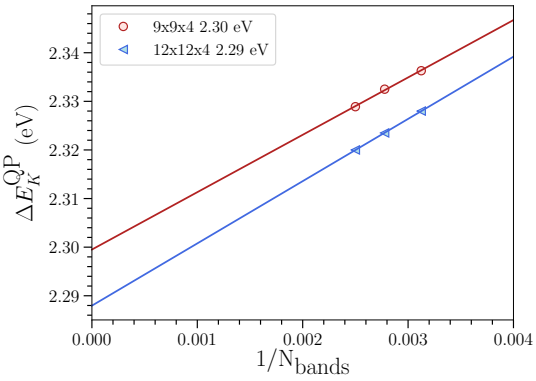

Figure 12: Extrapolated G_0W_0@PBE quasiparticle bandgap, E_K^{QP}, at the K point, in eV, for bulk WS_2, for different k-meshes as a function of the inverse number of bands, 1/N. The legend also displays the extrapolated quasiparticle bandgap for each k-mesh. The extrapolated gap at the larger k-mesh has been used as the fitting target for the SRSH calculations.

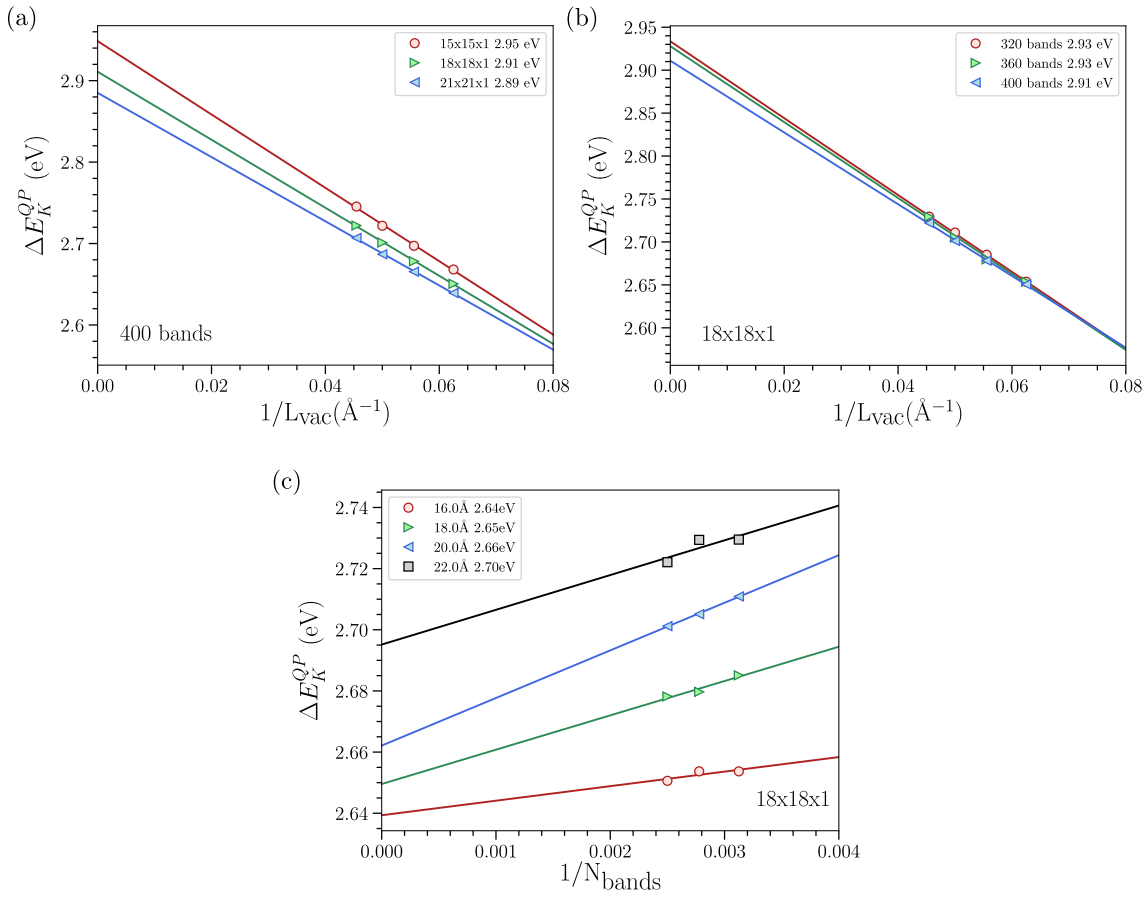

Figure 13: Extrapolated G_0W_0@PBE quasiparticle bandgap, E_K^{QP}, at the K point, in eV, for different k-meshes, for WS_2 monolayer (1L), as a function of the inverse vacuum distance for each k-mesh (a), different number of bands 1/N for a k-mesh (b), and different vacuum distances (c). The legend also displays the extrapolated quasiparticle bandgap. The extrapolated 2.66 eV with k-mesh $18 \times 18 \times 1$ is used as the target bandgap for the SRSH calculations.

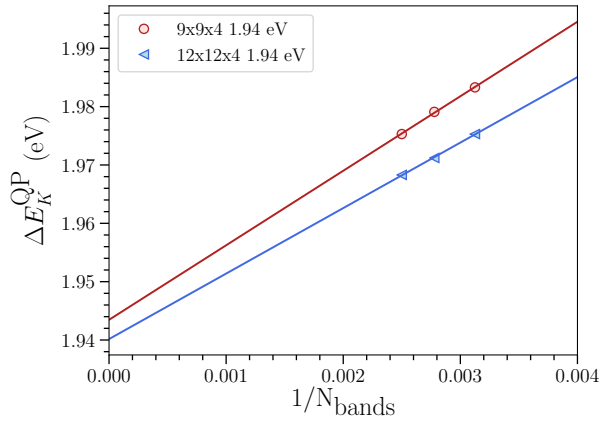

Figure 14: Extrapolated G_0W_0@PBE quasiparticle bandgap, E_K^{QP}, at the K point, in eV, for bulk WSe_2, for different k-meshes as a function of the inverse number of bands 1/N. The legend also displays the extrapolated quasiparticle bandgap given for each k-mesh. The extrapolated gap at the larger k-mesh has been used as the fitting target for the SRSH calculations.

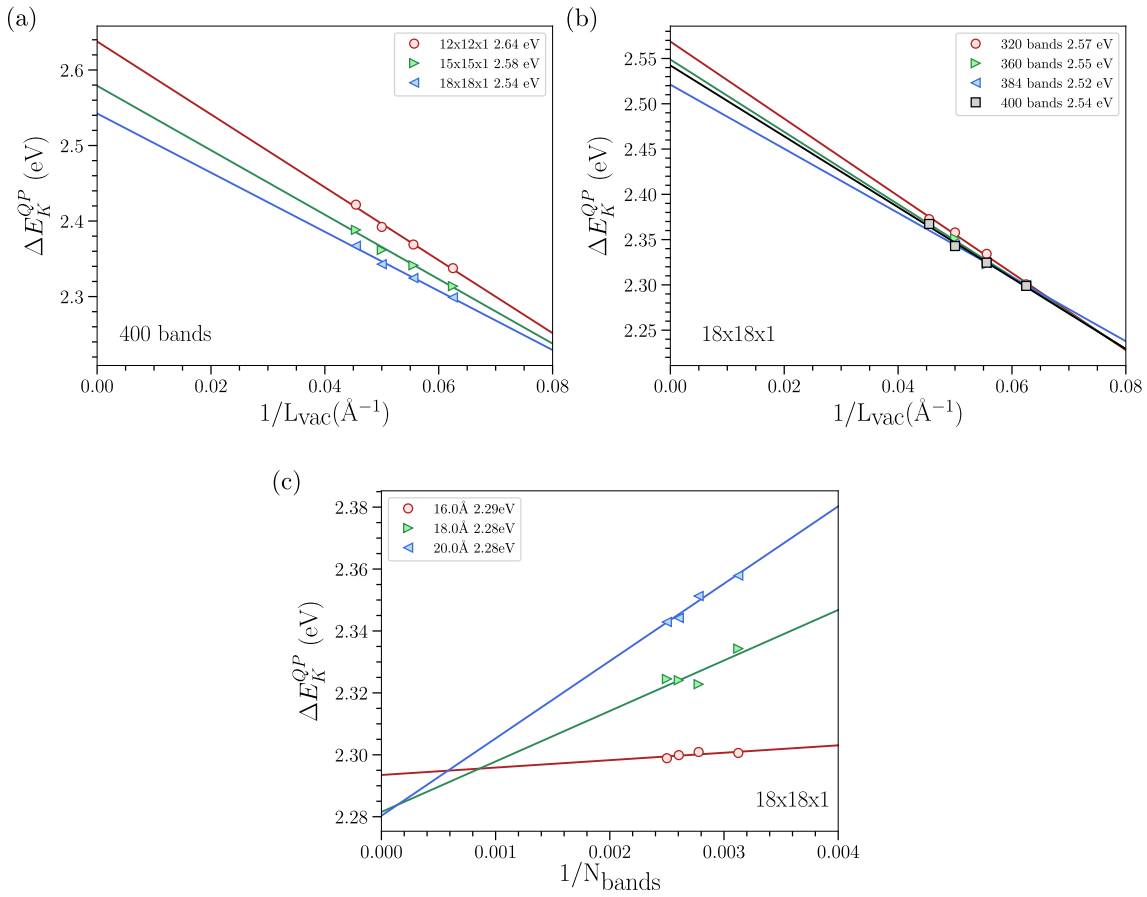

Figure 15: Extrapolated G_0W_0@PBE quasiparticle bandgap, E_K^{QP}, at the K point, in eV, for different k-meshes, for 1L WSe_2, as a function of the inverse vacuum distance for each k-mesh (a), different number of bands 1/N for a k-mesh (b), and different vacuum distances (c). The legend also displays the extrapolated quasiparticle bandgap. The extrapolated 2.28 eV with k-mesh $18 \times 18 \times 1$ is used as the target bandgap for the SRSH calculations.

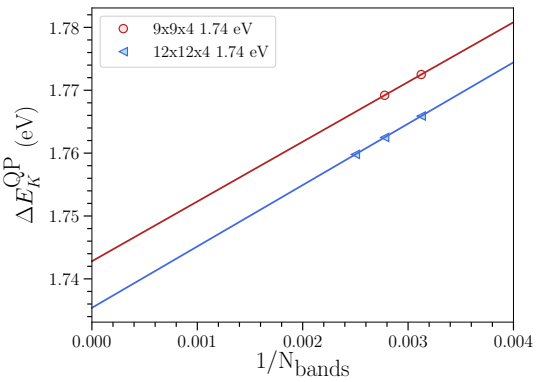

Figure 16: Extrapolated G_0W_0@PBE quasiparticle bandgap, E_K^{QP}, at the K point, in eV, for bulk $MoSe_2$, for different k-meshes as a function of the inverse number of bands 1/N. The legend also displays the extrapolated quasiparticle bandgap given for each k-mesh. The extrapolated gap at the larger k-mesh has been used as the fitting target for the SRSH calculations.

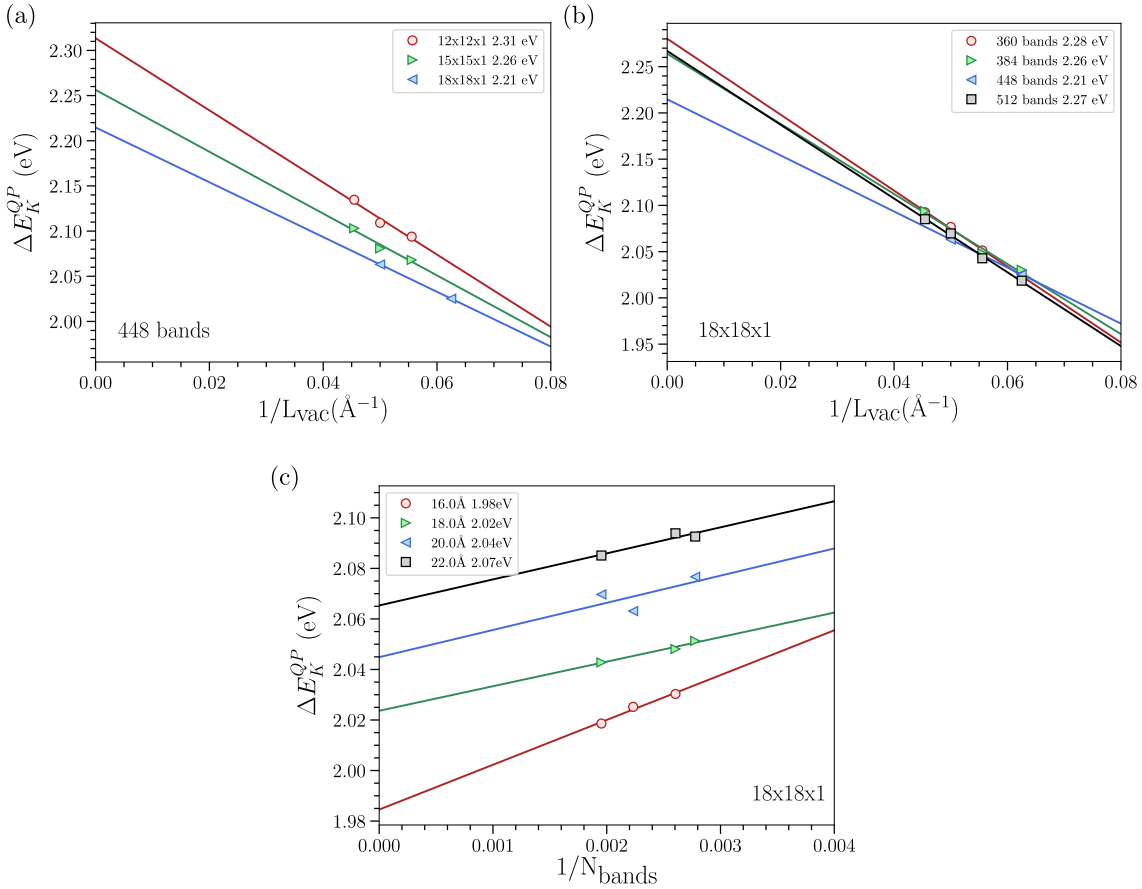

Figure 17: Extrapolated G_0W_0@PBE quasiparticle bandgap, E_K^{QP}, at the K point, in eV, for different k-meshes, for 1L $MoSe_2$, as a function of the inverse vacuum distance for each k-mesh (a), different number of bands 1/N for a k-mesh (b), and different vacuum distances (c). The legend also displays the extrapolated quasiparticle bandgap given for each k-mesh. The extrapolated 2.04 eV with k-mesh $18 \times 18 \times 1$ is used as the target bandgap for the SRSH calculations.

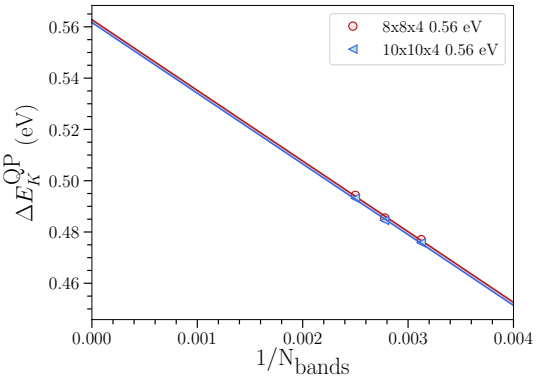

Figure 18: Extrapolated G_0W_0@HSE quasiparticle bandgap, E_K^{QP}, at the Γ point, in eV, for black phosphorus bulk, for different k-meshes as a function of the inverse number of bands 1/N. The legend also displays the extrapolated quasiparticle bandgap given for each k-mesh. The extrapolated gap 0.56 eV at the k-mesh $8 \times 8 \times 4$ has been used as the fitting target for the SRSH calculations.

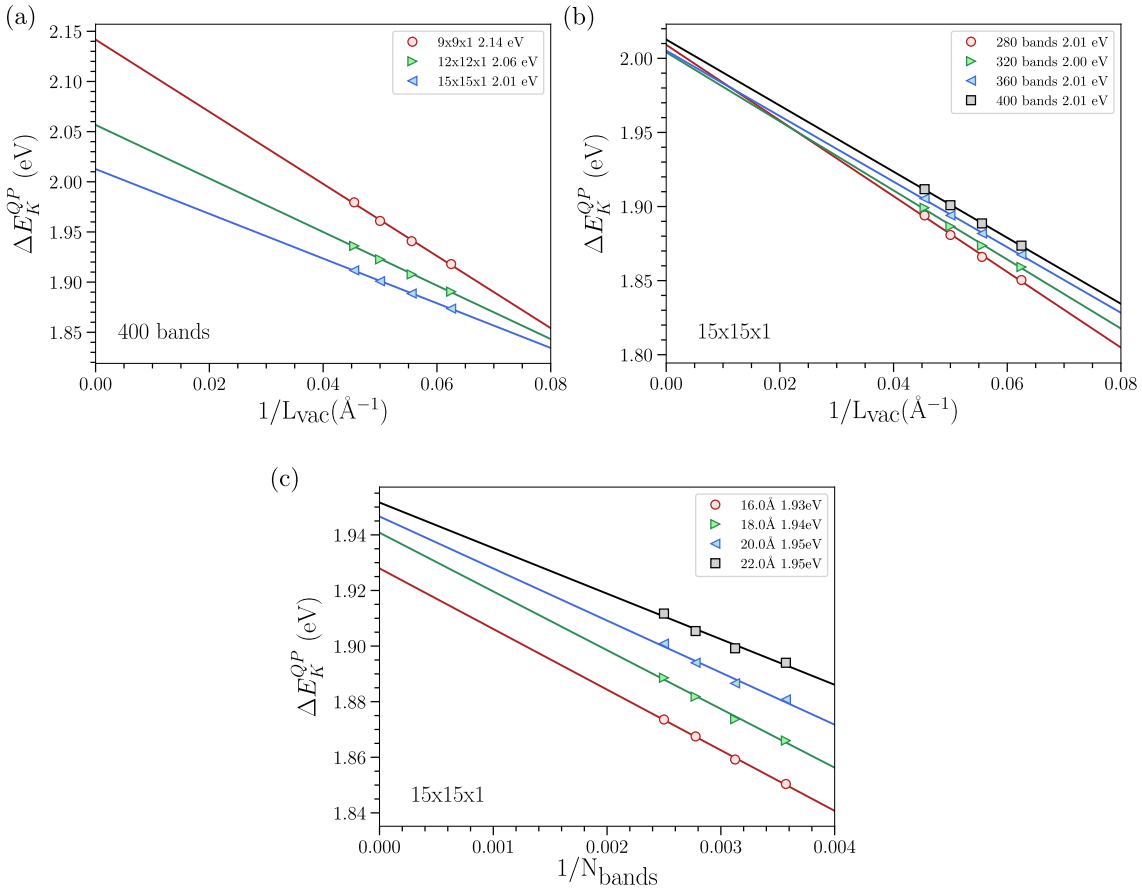

Figure 19: Extrapolated G_0W_0@HSE quasiparticle bandgap, E_K^{QP}, at the Γ point, in eV, for different k-meshes, for phosphorene, as a function of the inverse vacuum distance for each k-mesh (a), different number of bands 1/N for a k-mesh (b), and different vacuum distances (c). The legend also displays the extrapolated quasiparticle bandgap given for each k-mesh. The extrapolated 1.95 eV with k-mesh $15 \times 15 \times 1$ is used as the target bandgap for the SRSH calculations.

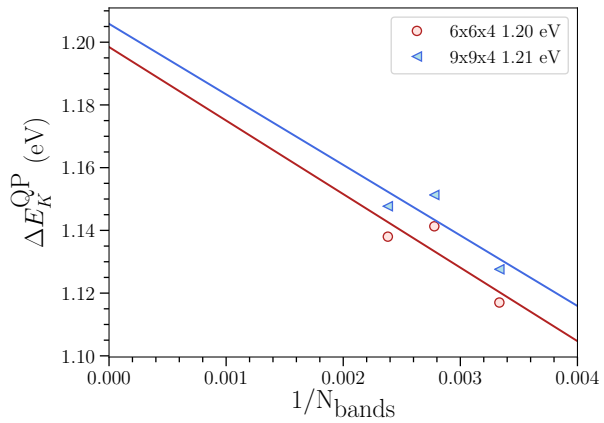

Figure 20: Extrapolated G_0W_0@PBE quasiparticle bandgap, E_K^{QP}, at the Γ point, in eV, for bulk InSe, for different k-meshes as a function of the inverse number of bands 1/N. The legend also displays the extrapolated quasiparticle bandgap given for each k-mesh. The extrapolated 1.21 eV with k-mesh $9 \times 9 \times 4$ is used as the target bandgap for the SRSH calculations.

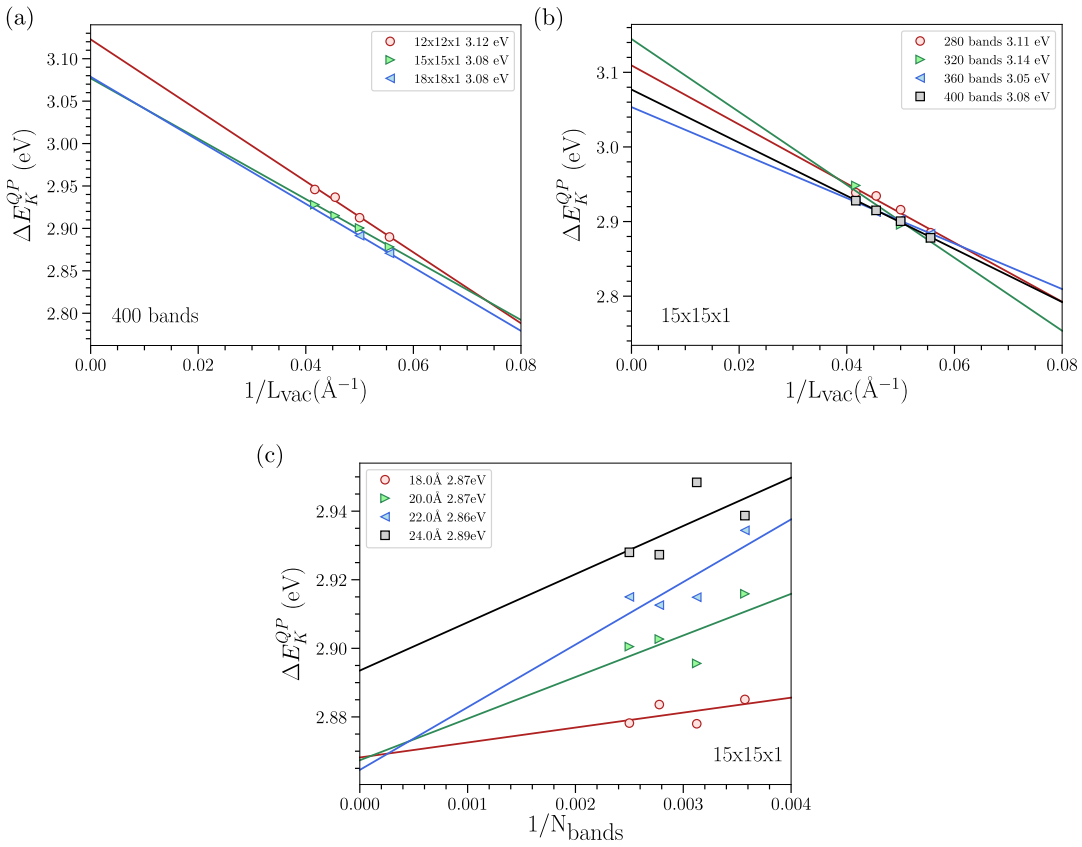

Figure 21: Extrapolated G_0W_0@PBE quasiparticle bandgap, E_K^{QP}, at the Γ point, in eV, for different k-meshes, for 1L InSe, as a function of the inverse vacuum distance for each k-mesh (a), different number of bands 1/N for a k-mesh (b), and different vacuum distances (c). The legend also displays the extrapolated quasiparticle bandgap. The extrapolated 2.87 eV with k-mesh $15 \times 15 \times 1$ is used as the target bandgap for the SRSH calculations.

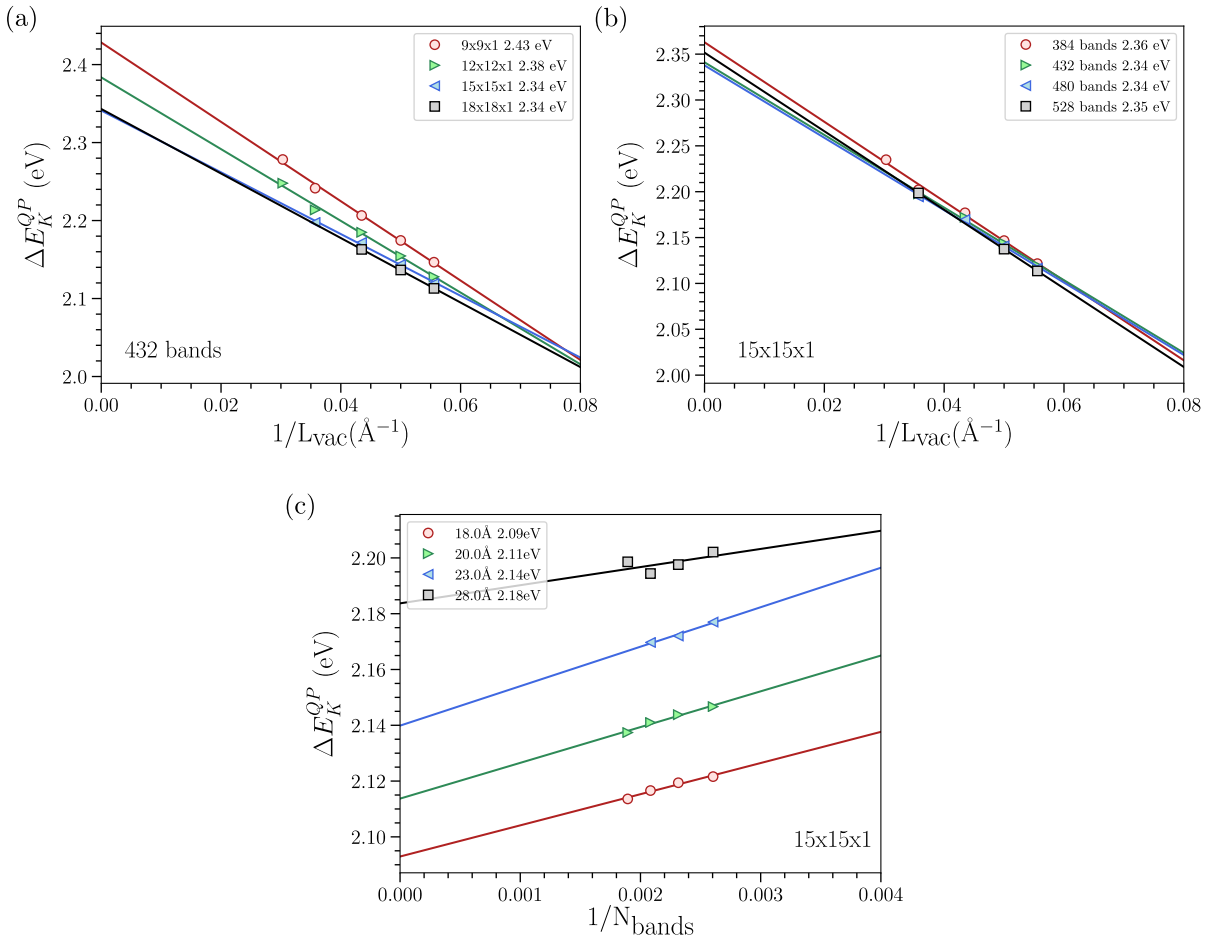

Figure 22: Extrapolated G_0W_0@LDA quasiparticle bandgap, E_K^{QP}, at the Γ point, in eV, for different k-meshes, for MoS_2 bilayer (2L), as a function of the inverse vacuum distance for each k-mesh (a), different number of bands 1/N for a k-mesh (b), and different vacuum distances (c). The legend also displays the extrapolated quasiparticle bandgap. The extrapolated 2.18 eV with k-mesh $15 \times 15 \times 1$ is used as the target bandgap for the SRSH calculations.

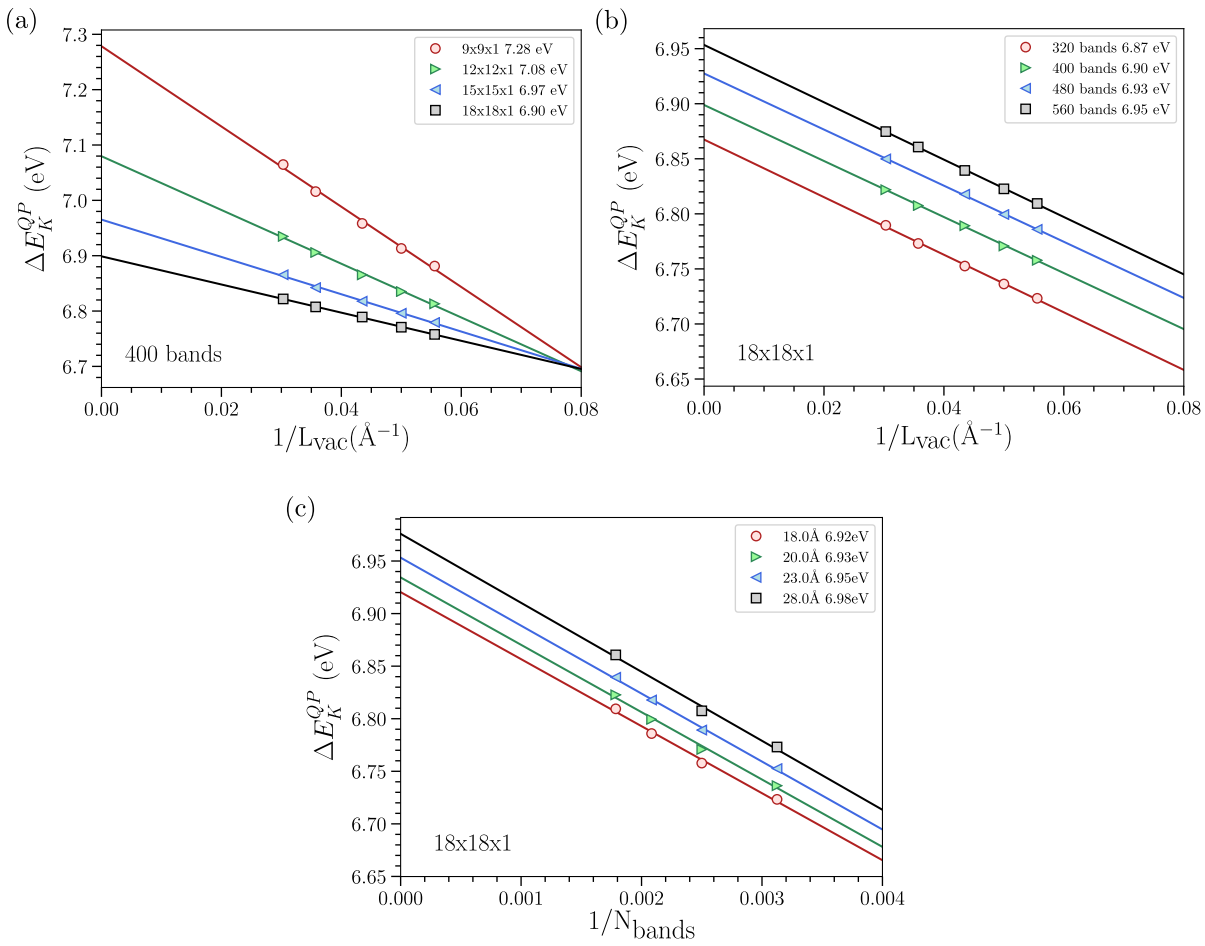

Figure 23: Extrapolated G_0W_0@LDA quasiparticle bandgap, E_K^{QP}, at the Γ point, in eV, for different k-meshes, for 2L h-BN, as a function of the inverse vacuum distance for each k-mesh (a), different number of bands 1/N for a k-mesh (b), and different vacuum distances (c). The legend also displays the extrapolated quasiparticle bandgap. The extrapolated 6.95 eV with k-mesh $18 \times 18 \times 1$ is used as the target bandgap for the SRSH calculations.

3.1.2 Gap Deviation Surfaces for Transition Metal Dichalcogenides

In this section we provide the gap deviation surfaces obtained following the procedure explained in Sec. 2 of the main text for the transition metal dichalcogenides WS_2, WSe_2 and $MoSe_2$, projections of which are shown in Fig. 1.

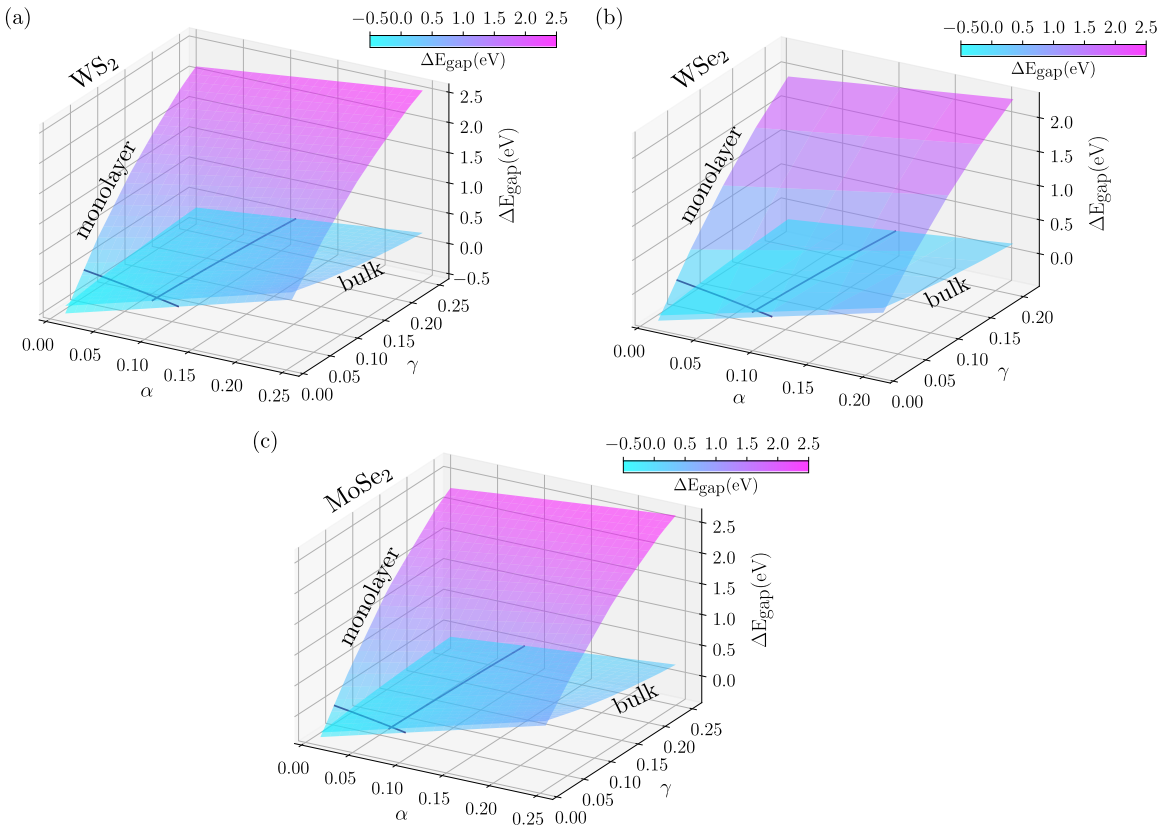

Figure 24: Gap deviation surfaces, $\Delta E_{gap} = E_{gap}^{SRSH} - E_{gap}^{GW}$, obtained for (a) WS_2, (b) WSe_2, and (c) $MoSe_2$.

3.1.3 Transition-Metal Dichalcogenides

WS_2, WSe_2, and $MoSe_2$ are semiconductors that crystallize in the trigonal prismatic 2H phase (space group $P\bar{3}m1$) in their ground state. Figure 25 (a-c) displays contour plots of the error in the band gap, ΔE_g, for bulk and monolayers of the three materials. Interestingly, the errors in the band gap present similar trends across this group of materials: the bulk phases exhibit a very small degree of acceptable variation in the fraction of short-range exact exchange, α, whereas this parameter can vary more widely for monolayers. It is also clear from these figures that optimizing the SRSH for just one phase can lead to rather large errors for the other phase. For example, selecting acceptable values of (α, γ) for bulk WS_2 at the extremes of the $\alpha - \gamma$ plot (Fig. 25a) leads to large errors in the predicted band gap of the monolayer, ranging from -0.122 eV for $(\alpha, \gamma) = (0.102, 0.010\,\text{Å}^{-1})$ to 2.33 eV for $(\alpha, \gamma) = (0.116, 0.248\,\text{Å}^{-1})$. Conversely, optimizing the SRSH purely for monolayer WS_2 results in errors in the bulk band gap ranging from 0.030 eV for

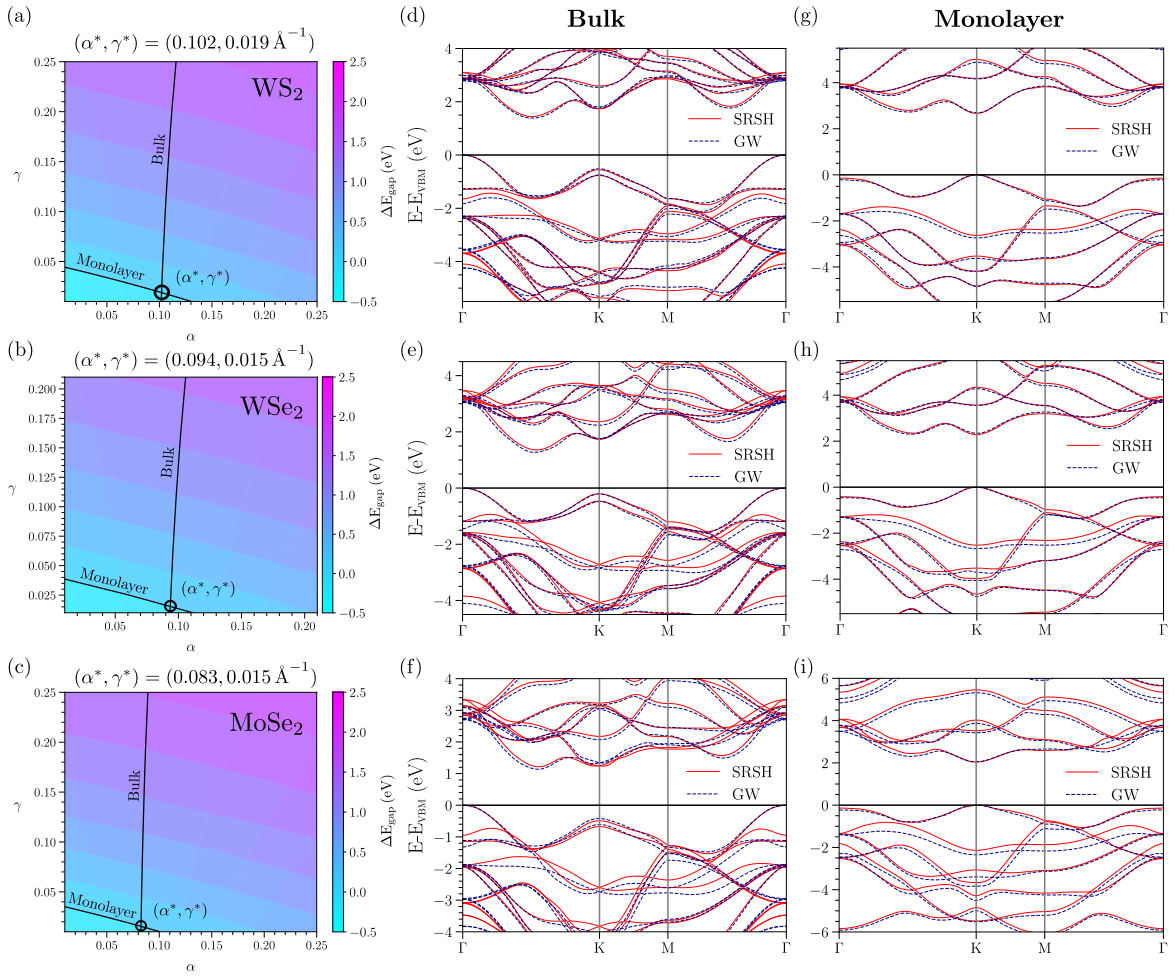

Figure 25: (a)-(c) Contour maps of the gap deviation, ΔE_g, for WS_2, WSe_2, and $MoSe_2$. The solid black lines represent the values for which $\Delta E_g = 0$ for bulk and monolayer structures, and the intersection of the two lines yields a unique set of values (α^*, γ^*) that are transferable between the bulk and monolayer. (d)-(f) Bandstructures for bulk and (g)-(i) bandstructures for monolayers of WS_2, WSe_2, and $MoSe_2$ from SRSH (solid lines) and G_0W_0@PBE (dashed lines). Here and throughout, special points in the Brillouin zone are defined explicitly in section S4 of the SM. γ has units of Å^{-1}.

$(\alpha, \gamma) = (0.011, 0.044\,\text{Å}^{-1})$ to 0.049 eV for $(\alpha, \gamma) = (0.113, 0.010\,\text{Å}^{-1})$. The point of intersection of the zero-crossings of the gap deviation surfaces $(\alpha^*, \gamma^*) = (0.102, 0.019\,\text{Å}^{-1})$, simultaneously renders the error in the band gap zero for both phases. Similar behavior is observed for WSe_2 and $MoSe_2$.

Table 3 displays the optimal parameters, α^* and γ^*, along with the RPA dielectric constants, ϵ_∞, as well computed GW, GW-BSE, SRSH, and TD-SRSH results. Our GW and GW-BSE results are in good agreement with past literature - see Tables I and II in the SM Section S5 for a detailed comparison. Figure 25 displays the corresponding SRSH bandstructures along with the corresponding GW bandstructures. As the SRSH functionals were tuned to reproduce GW band gaps extrapolated to infinite interlayer separation and infinite k-point sampling (see SM), the outcome of a particular un-extrapolated GW calculation will always differ to some extent from the SRSH result. For example, for WS_2, the un-extrapolated GW band gap for the monolayer (at the K point) is 40 meV larger than the SRSH band gap and the un-extrapolated GW band gap for the bulk (at the K point) is 30 meV larger than its SRSH counterpart. Similar differences ($\sim$ 20 meV) are found for $MoSe_2$ and WSe_2. The above small differences notwithstanding, Figure

Table 1: Brillouin zone sampling, tuned SRSH parameters (α^*, γ^*), average inverse macroscopic dielectric constant (ϵ_∞^{-1}), GW band gap (E^{GW}), GW-BSE optical gap ($E_{\mathrm{opt}}^{\mathrm{GW\text{-}BSE}}$), SRSH band gap ($E^{\mathrm{SRSH}}$, fitted to an extrapolated GW quasiparticle band gap), and TD-SRSH optical gap ($E_{\mathrm{opt}}^{\mathrm{TD\text{-}SRSH}}$), for the various materials studied in this article. Additional computational details are given in the SM. Band gaps and optical gaps are calculated at the K point for the TMDC materials (WS_2, WSe_2, $MoSe_2$) and at the Γ point for black phosphorus (BP) and InSe.

Material	Phase	**k**-grid	α^*	γ^*(Å^{-1})	ϵ_∞^{-1}	E^{GW} [eV]	$E_{\mathrm{opt}}^{\mathrm{GW\text{-}BSE}}$ [eV]	E^{SRSH} [eV]	$E_{\mathrm{opt}}^{\mathrm{TD\text{-}SRSH}}$ [eV]
WS_2	Bulk	$12 \times 12 \times 4$	0.102	0.019	0.093	2.32	2.22	2.29	2.21
	1L	$18 \times 18 \times 1$			1.0	2.70	2.29	2.66	2.32
WSe_2	Bulk	$12 \times 12 \times 4$	0.094	0.015	0.084	1.97	1.91	1.94	1.89
	1L	$18 \times 18 \times 1$			1.0	2.34	1.98	2.28	1.99
$MoSe_2$	Bulk	$12 \times 12 \times 4$	0.083	0.015	0.079	1.76	1.70	1.74	1.74
	1L	$18 \times 18 \times 1$			1.0	2.06	1.72	2.04	1.78
BP	Bulk	$8 \times 8 \times 4$	0.170	0.035	0.095	0.49	0.40	0.56	0.32
	1L	$15 \times 15 \times 1$			1.0	1.89	1.37	1.95	1.38
InSe	Bulk	$9 \times 9 \times 4$	0.149	0.021	0.121	1.15	1.05	1.21	1.10
	1L	$15 \times 15 \times 1$			1.0	2.90	2.67	2.87	2.76

25 (d-f) shows very good agreement between the GW and SRSH bandstructures for all three, especially at the band edges. Qualitatively, the deviations are somewhat larger for the bulk than for the monolayers, particularly for the selenides. These deviations also become more apparent deeper into the valence or conduction band, which is generally expected when using SRSH eigenvalues as approximate quasi-particle excitation energies [61], [114], [115]. These deeper bands, however, are less relevant to electronics applications or to the low-energy optical absorption spectrum. The mean absolute deviation between the GW and SRSH results for the top-most valence band and bottom-most conduction band, over all k points, is 0.060 eV, 0.063 eV and 0.103 eV for monolayer WS_2, WSe_2 and $MoSe_2$, respectively, and 0.059 eV, 0.074 eV and 0.098 eV for the bulk.

We note that the parameter γ is relatively small and similar to the value for MoS_2 reported in Ref. [56]. As a consequence, one might be tempted to conclude that the SRSH functional behaves almost as the corresponding limit of a global hybrid [116]. However, in the $\gamma \to 0$ limit, β would be irrelevant and the exchange would be asymptotically screened by $1/\alpha$ instead of ϵ_∞, with consequences for predicted exciton binding energies. For example, in Chen *et al.* [65], the fraction of exact exchange was tuned to fulfill the ionization potential theorem in a system with a defect. It was concluded in that work that using a global hybrid that is tuned to the band gap at only one k-point may lead to inaccurate electronic structure predictions. This underscores the importance of using a range-separated hybrid rather than a global one.

Next, we consider optical absorption spectra for the same materials, as shown in Figure 26. These calculations were performed without spin-orbit coupling, primarily due to the computational cost of the reference GW-BSE calculations. Insets provide corresponding TD-SRSH spectra for monolayers that do include spin-orbit coupling. Recalling that SRSH parameters are only tuned to reproduce the GW band gap at a single k-point, any further calculations with the same parameters are true tests of the predictive capability of the functional. As seen in Figure 26, the overall agreement between the GW-BSE and TD-SRSH spectra is highly satisfactory, especially for the low-energy part of the spectrum. At higher energies ($\gtrsim$ 2.5 eV), some disagreement becomes more apparent, most likely due to the above-noted larger deviations between higher and lower lying SRSH and GW eigenvalues. Nonetheless, the agreement between GW-BSE and TD-

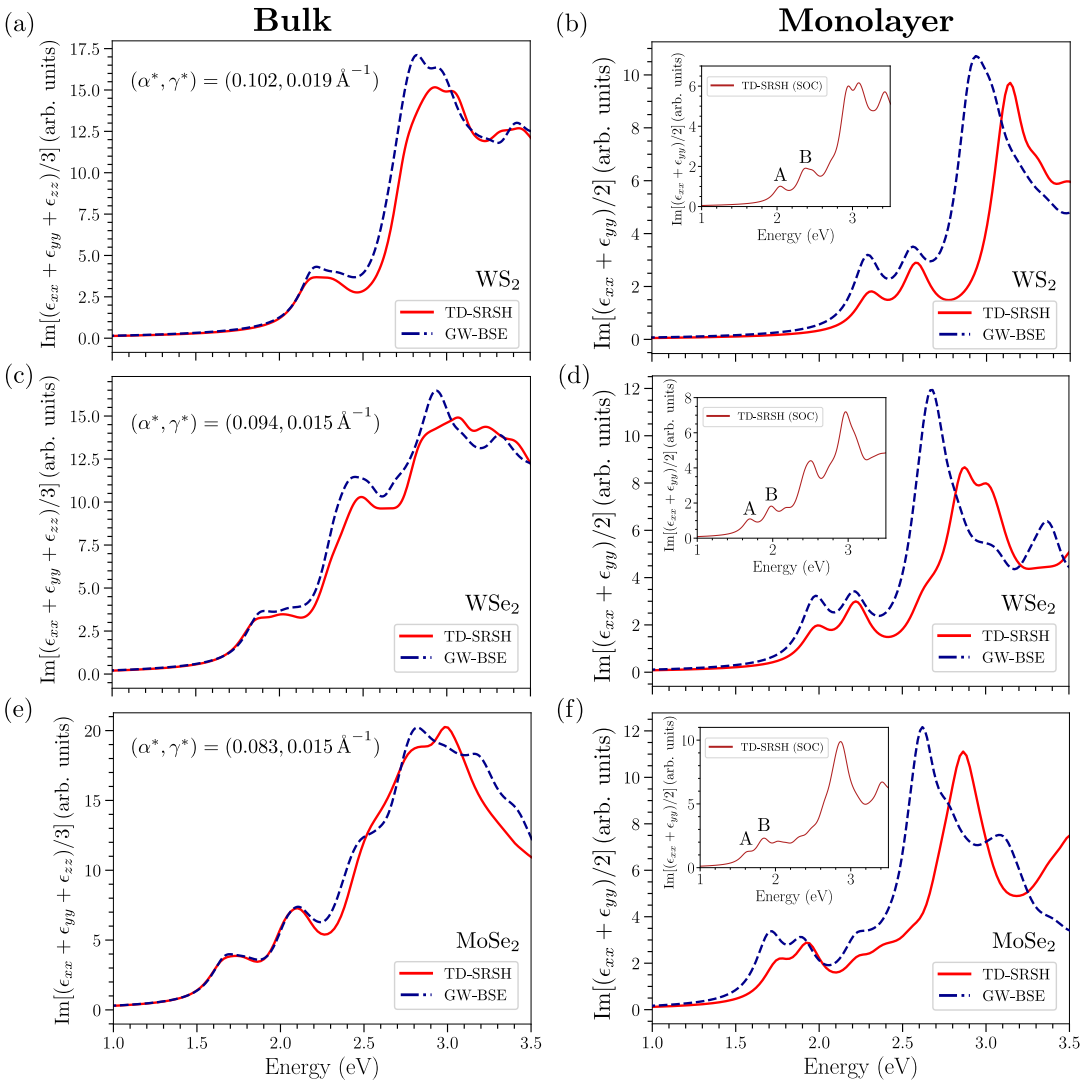

Figure 26: Optical absorption spectra calculated, without spin-orbit coupling, using TD-SRSH (red solid line) and GW-BSE (blue dashed line). Rows corresponds to WS_2, WeS_2, and $MoSe_2$. Results for the bulk and for the monolayer are given in the left and right columns, respectively. Insets: corresponding monolayer SRSH calculations that include spin-orbit coupling, in which the A and B peaks represent excitons of the TMDCs. See Table 3 for specific parameters.

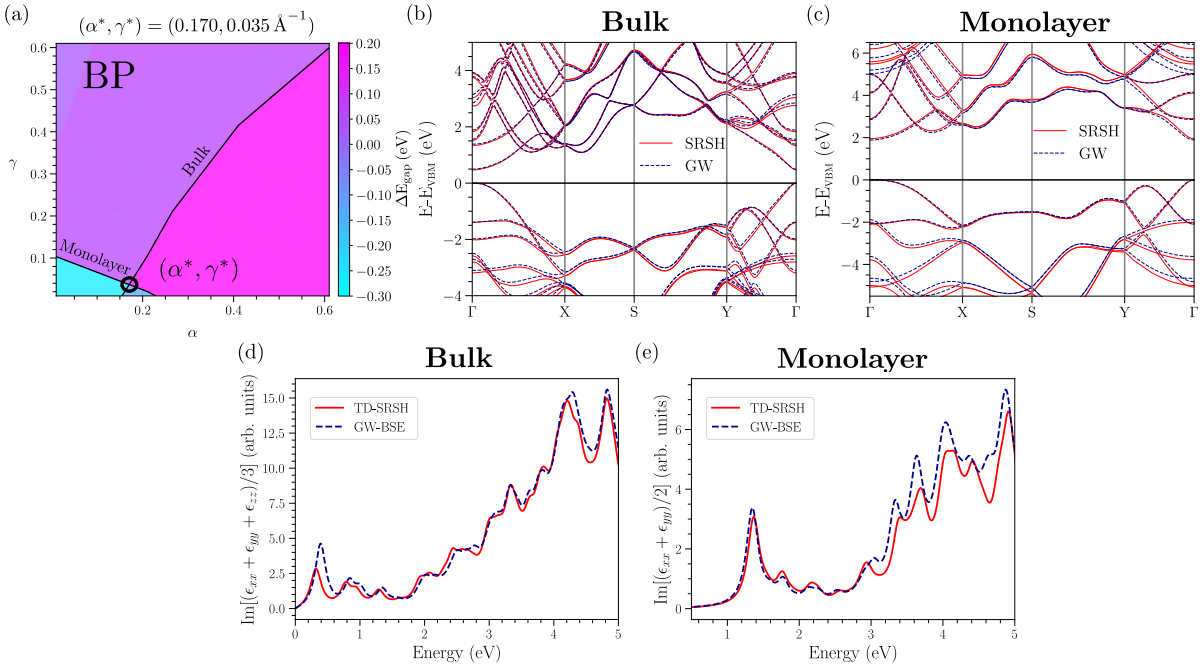

Figure 27: (a) Gap deviation, ΔE_g, exhibited as a color map in the $\alpha - \gamma$ plane, for black phosphorus. The solid black lines represent the values for which $\Delta E_g = 0$ for bulk and monolayer structures, and the intersection of the two lines yields a unique set of values (α^*, γ^*) that are transferable between the bulk and monolayer. (b) Bandstructures for bulk and (c) monolayers of black phosphorus from SRSH (solid lines) and G_0W_0@PBE (dashed lines). (d) Optical absorption spectra for bulk and (e) monolayers of black phosphorus from TD-SRSH (solid red lines) and G_0W_0-BSE (dashed-dotted blue lines). γ has units of Å^{-1}.

SRSH spectra is particularly good for the bulk, and the neglecting of the anisotropy of the dielectric constant does not seem to have introduced qualitative failures in the monolayer calculations. For the latter, the positions of the low-energy peaks are generally in good agreement between TD-SRSH and GW-BSE (deviations smaller than 0.1 eV) whereas the discrepancy in peak heights is more apparent.

Upon inclusion of spin-orbit coupling in the SRSH monolayer calculations, we observe the appearance of the characteristic A and B excitonic peaks of TMDC monolayers. For WS_2, the experimentally measured A and B peaks are at 2.12 eV and 2.5 eV [117], respectively, which compares excellently to the TD-SRSH peaks located at 2.05 eV and 2.38 eV. Likewise, for WSe_2, the experimental values are 1.74 eV and 2.16 eV [118], compared to TD-SRSH values at 1.70 eV and 1.98 eV, which represents a slightly larger, but still small, deviation. Lastly, for $MoSe_2$, the experimentally measured A and B peaks are at 1.64 eV and 1.83 eV [119], respectively, while the TD-SRSH peaks are located at 1.63 eV and 1.85 eV.

3.1.4 Black Phosphorus and Phosphorene

Among the allotropes of phosphorus, black phosphorus (BP) is one of the most stable forms under ambient conditions [120]. In its ground state, BP is composed of puckered monolayers arranged in an AB stacked structure (space group 64, Cmce) and is very sensitive to changes in pressure [121], [122]. It is also characterized by strong in-plane anisotropy that provides an opportunity for exploiting its orientation-dependent opto-electronic properties in a variety of applications [122]–[124]. The band gap of BP varies

from about 0.3 eV in the bulk to around 2.0 eV for the monolayer (phosphorene), covering much of the range between semiconducting TMDCs and gapless graphene [122], [123], [125].

Because BP is a narrow-gap semiconductor, semilocal functionals such as PBE [104] predict an incorrect metallic ground state for this material, creating a qualitatively incorrect starting point for "single-shot" GW calculations [126]–[128]. Therefore, here we employed the HSE06 short-range hybrid functional [102], [103] to produce a gapped (0.317 eV direct gap at Γ [129]) starting point for the GW calculation. The use of hybrid functionals as a starting point for perturbative GW calculations is a topic of ongoing research (e.g., [8], [31], [128], [130]–[132]). In the present case, this approach yielded a G_0W_0@HSE extrapolated band gap of 0.56 eV, in good agreement with Refs. [132], [133].

Figure 27(a) displays contour plots of the error, ΔE_g, in the SRSH band gap relative to the GW (G_0W_0@HSE) fitting target (see SM for details). The zero crossing lines of the ΔE_g surfaces for BP and phosphorene intersect at $(\alpha^*, \gamma^*) = (0.170, 0.035\,\text{Å}^{-1})$, which furnishes the optimal set of parameters for further SRSH/TD-SRSH calculations. The complete set of parameters is listed in Table 3.

Using these parameters, Figures27(b, c) and 27(d, e) display corresponding band structures and optical absorption spectra for BP and phosphorene. Once again, owing to the tuning to extrapolated GW band gaps, there is a small deviation between un-extrapolated GW and SRSH values, but beyond that, once again we find excellent agreement between the GW and SRSH bandstructures, both for BP and phosphorene, not just at the band edges but also up to ~ 2 eV into the valence and conduction bands. Again, the mean absolute deviation for the highest valence band and lowest conduction band across the entire Brillouin zone is a mere 0.054 eV for the bulk phase and 0.071 eV for the monolayer. For the optical spectra, we find excellent agreement between the two approaches, with deviations in peak positions being at most 60 meV in the low-energy part of the spectrum ($\lesssim 2.5$ eV). The first excitonic peak for phosphorene is located at 1.37 eV, in agreement with a previous BSE study [125]. Here, TD-SRSH and GW-BSE peak heights are also in better agreement than for the TMDCs.

3.1.5 Indium Selenide

As a final example, we consider β-InSe (space group $P6_3/mmc$). This is a transition-metal monochalcogenide that is part of a larger group of similar materials composed of a Group IIIA element (In, Ga) and a chalcogen (S, Se, Te) [134]. This material exhibits a band gap that changes from 2.87 eV (indirect gap) for a monolayer (theoretical) [135] to 1.20-1.28 eV (direct gap) for the bulk [136]–[138], as well as high-carrier mobility [134], [139], making it a desirable candidate for optoelectronics [134], [140]–[142].

Figure 28(a) display the contour plots of the gap deviation, ΔE_g, in the SRSH band gap relative to the GW fitting targets for the bulk and monolayer structures (see SM). Similar to the TMDCs, we observe that bulk phase exhibits a very small degree of acceptable variation in the fraction of short-range exact exchange, α, whereas this parameter can vary more widely for the monolayer. The optimal set of SRSH parameters, $(\alpha^*, \gamma^*) = (0.149, 0.021\,\text{Å}^{-1})$, is again obtained from the point of intersection of the zero-crossing lines of the ΔE_g surfaces for bulk and monolayer InSe. The complete set of parameters for InSe is listed in Table 3. Using this tuned SRSH functional, Figure 28(b, c) shows the bandstructures of bulk and monolayer InSe, along with reference bandstructures from GW calculations. Once again, owing to extrapolation the SRSH gaps differ

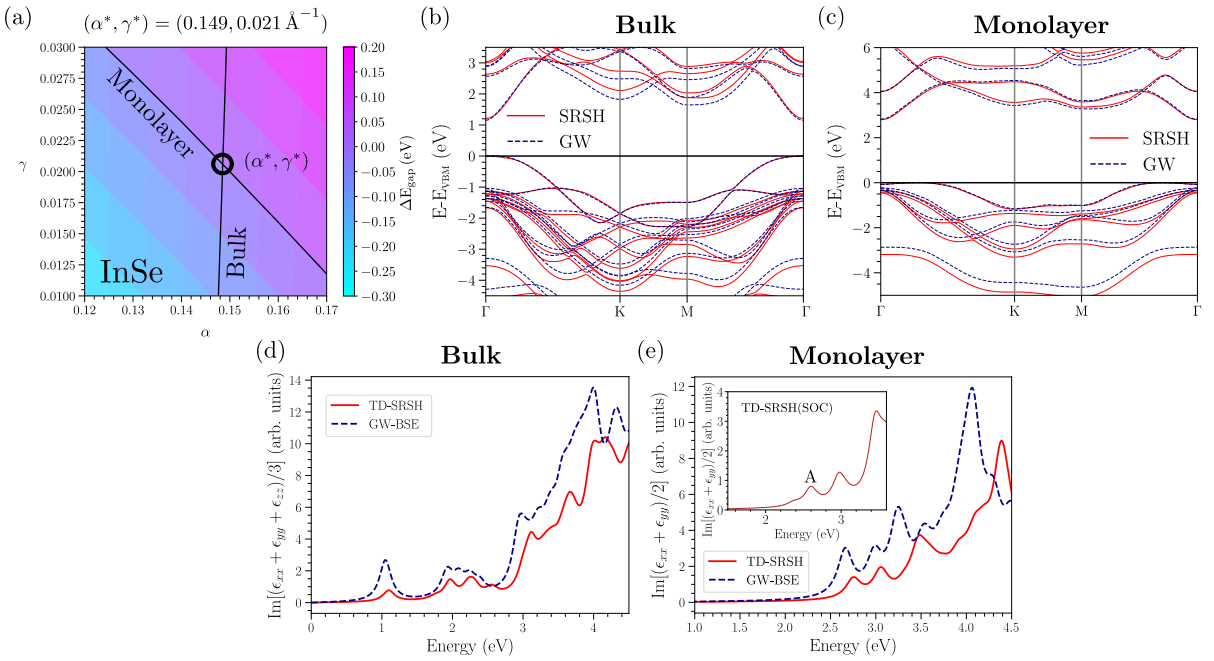

Figure 28: (a) Gap deviation, ΔE_g, exhibited as a color map in the $\alpha - \gamma$ plane, for InSe. The solid black lines represent the values for which $\Delta E_g = 0$ for bulk and monolayer structures, and the intersection of the two lines yields a unique set of values (α^*, γ^*) that are transferable between the bulk and monolayer. (b) Bandstructures for bulk and (c) monolayers of black phosphorus from SRSH (solid lines) and G_0W_0@PBE (dashed lines). (d) Optical absorption spectra for bulk and (e) monolayers of InSe from TD-SRSH (solid red lines) and G_0W_0-BSE (dashed-dotted blue lines). γ has units of Å^{-1}.

from the GW ones by 60 meV for the bulk and 30 meV for the monolayer. As seen in the figure, the agreement between the SRSH and GW bandstructures is quite satisfactory across the chosen high-symmetry paths, with a mean absolute deviation for the top valence band and the bottom conduction band of 0.163 eV for the bulk and 0.085 eV for the monolayer.

TD-SRSH optical absorption spectra for bulk and monolayer InSe are displayed in Figure 28(d, e), along with reference GW-BSE spectra. The TD-SRSH and GW-BSE spectra are in good agreement below ~ 3 eV with the largest error in the energies of the first two peaks being of the order of 0.2 eV, albeit with some differences in the oscillator strength. The agreement between the TD-SRSH and GW-BSE optical spectra is not as good above 3 eV. The remaining discrepancies may be partly due to computational limitations in k-point sampling in the GW calculations. The inset of Figure 28(e) displays the TD-SRSH absorption spectrum for the monolayer with the inclusion of spin-orbit coupling; the first excitonic peak (labeled A) appears at 2.6 eV, and agrees well with the value of ~ 2.57 eV reported in Ref. [143].

3.1.6 Assessment of SRSH Functionals for Bilayer MoS_2 and h-BN

Motivated by the promising results of the SRSH/TD-SRSH approach for bulk and monolayer structures, we now seek to understand how well these functionals perform for bilayers of vdW materials. In general, one could expect that as long as the characteristic length scale for switching from short-range exact exchange (α) to long-range exact exchange ($1/\epsilon_\infty$), namely $1/\gamma$, is greater than the thickness (t) of the bilayer/few-layer slab, the interaction between two charges separated across the slab thickness will be governed

largely by the (tuned) short-range exchange. In this scenario, it is reasonable to hypothesize that the SRSH/TD-SRSH formalism ought to retain its accuracy for bilayer/few-layer structures, even when merely employing the simply functional form of the SRSH with asymptotic long-range screening of $\epsilon_\infty = 1$. In the following, we test this hypothesis for bilayer MoS_2 and h-BN, bulk and monolayers of which were studied previously in Ref. [56].

3.1.7 MoS_2

Tuned SRSH parameters, (α^*, γ^*), for bulk and monolayer MoS_2 were reported previously in Ref. [56] and are listed in Table 4. In principle, one could use these parameters directly to make a *prediction* for bilayer MoS_2. It is also possible to re-tune the SRSH using bilayer MoS_2 and the bulk as reference structures. To this end, we first perform GW calculations for MoS_2 bilayers to determine the reference quasiparticle band gaps (see SM and Table 4). We then apply our tuning procedure (Section 2.2) to obtain the error, ΔE_g, for the bilayer as a function of α and γ. Figure 29(a) display the ΔE_g contour plots for monolayer, bilayer, and bulk MoS_2. As seen in the figure, the optimal parameters for the bilayer and bulk, labeled α' and γ', are not identical to those of the monolayer and bulk (α^*, γ^*). Specifically, α' and α^* do not vary substantially, as the bulk constrains these values to a rather small window, and the main distinction is manifested in the values of γ' and γ^*. In addition, the ΔE_g surfaces of the monolayer and bilayer and, consequently, the zero-crossing lines are nearly parallel to each other. This indicates that it is not possible to render $\Delta E_g = 0$ simultaneously for the monolayer and bilayer, though this does not rule out simultaneous minimization of a different metric, an issue we do not explore further here.

Figures 29(b, c) display the SRSH bandstructure and TD-SRSH optical absorption spectrum for bilayer MoS_2, using the optimal values of α' and γ', along with their GW and GW-BSE counterparts. As before, there is an intrinsic 20 meV extrapolation difference. The overall agreement between the two approaches is excellent: the mean absolute error in the energy eigenvalues, considering the lowermost conduction band and the uppermost valence band, is a mere 0.087 eV. Similarly, we also find good agreement between the GW-BSE and TDSRSH optical spectra (Fig. 29(c)) with differences of less than 0.1 eV in peak positions for the low-energy part of the spectrum ($\lesssim 2.5$ eV). The inset of Figures 29(c) displays the TD-SRSH absorption spectrum with spin-orbit coupling included. We observe the characteristic splitting of the valence band into A and B excitonic peaks at 1.88 eV and 2.23 eV, respectively, that are in excellent agreement with the reported experimental values of 1.91 eV (A peak) and 2.12 eV (B peak) [144].

Returning to the issue of the transferability of the SRSH functional, we sought to understand the implications of modeling the MoS_2 bilayer using a functional specifically tuned for the monolayer and bulk (parameters α^* and γ^*), and conversely, modeling the monolayer using a functional specifically tuned for the bilayer and bulk (parameters α' and γ'). Figures 30 (a) present the outcome of such a comparison for the bilayer, bulk, and monolayer, with Figures 30 (b) displaying the corresponding TD-SRSH spectra. For the bulk structure, we find that the bandstructure and optical spectrum is essentially insensitive to the choice of parameters, as may be expected given that both sets of values are optimal for bulk MoS_2 ($\Delta E_g = 0$). For the monolayer and bilayer, using the non-optimal set of parameters leads to nearly rigid shifts of the bandstructure by ~ 0.5 eV. The optical absorption spectra display lower sensitivity to this choice of parameters. For

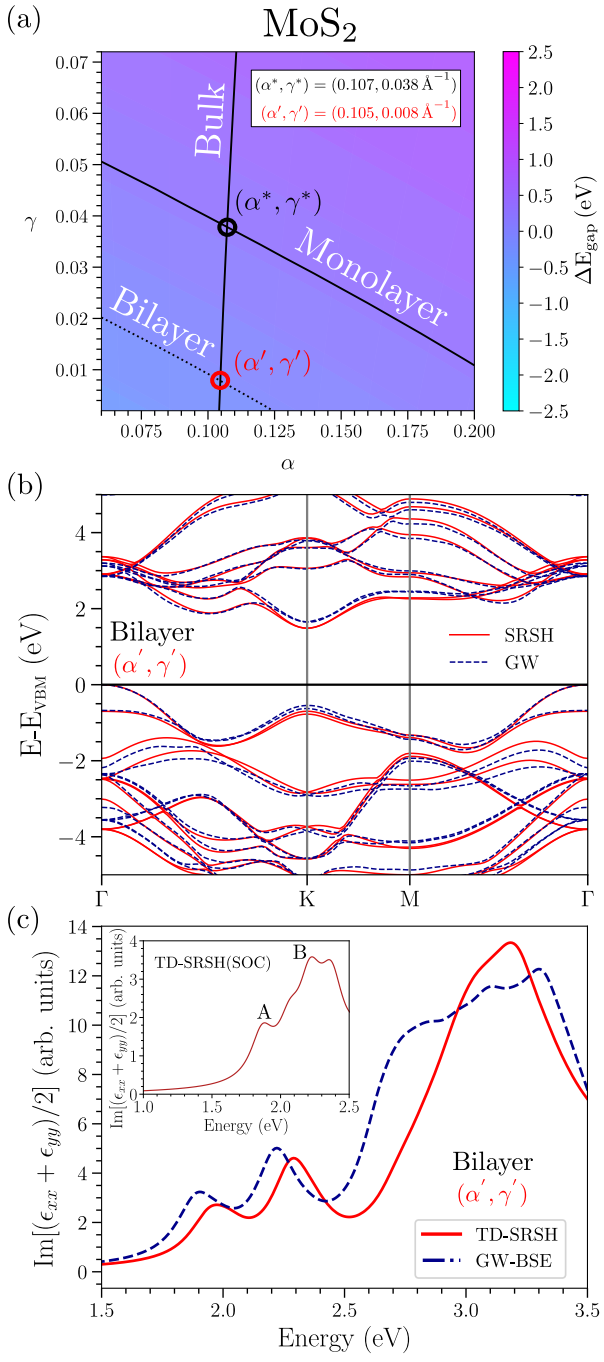

Figure 29: (a) 2D contour plots of the gap deviation, ΔE_g, for monolayer, bilayer, and bulk MoS_2. Solid black lines represent values for which $\Delta E_g = 0$. The intersections of the solid lines yield a set of values (α^*, γ^*) that are transferable between the monolayer and bulk, and a somewhat different set of values (α', γ') that are transferable between the bilayer and bulk. (b) Bandstructures for bilayer MoS_2 from SRSH (red solid lines), using the parameters (α', γ'), and from G_0W_0@PBE (blue dashed lines). (d) Optical absorption spectra for bilayer MoS_2 obtained with TD-SRSH (red solid line) and GW-BSE (blue dashed line). γ has units of $Å^{-1}$.

Table 2: Brillouin zone grid, tuned SRSH parameters (α^*, γ^*) for bulk-monolayer, tuned SRSH parameters (α', γ') for bulk-bilayer, average inverse macroscopic dielectric constant (ϵ_∞^{-1}), GW band gap (E^{GW}), GW-BSE optical gap $(E_{\text{opt}}^{\text{GW-BSE}})$, SRSH band gap $(E^{\text{SRSH}}$, fitted to an extrapolated GW quasiparticle band gap) and TD-SRSH optical gap $(E_{\text{opt}}^{\text{TD-SRSH}})$ MoS_2 and h-BN. Additional computational details for the calculations are given in the SM. Band gaps and optical gaps are calculated at the K point for all phases.

Material	Phase	**k**-grid	α^*	γ^*(Å^{-1})	α'	γ'(Å^{-1})	ϵ_∞^{-1}	E^{GW} [eV]	$E_{\text{opt}}^{\text{GW-BSE}}$ [eV]	E^{SRSH} [eV]	$E_{\text{opt}}^{\text{TD-SRSH}}$ [eV]
MoS_2	Bulk	$12 \times 12 \times 4$[a]					0.085	2.07[a]	2.00[a]	2.03[a]	1.91
	2L	$15 \times 15 \times 1$	0.107	0.038	0.105	0.008	1.0	2.20	1.90	2.18	1.97
	1L	$18 \times 18 \times 1$[a]					1.0	2.50[a]	2.00[a]	2.65[a]	2.02
h-BN	Bulk	$12 \times 12 \times 4$[a]					0.25	6.58[a]	5.48[a]	6.66[a]	5.82
	2L	$18 \times 18 \times 1$	0.201	0.072	0.204	0.041	1.0	6.79	5.29	6.95	5.91
	1L	$18 \times 18 \times 1$[a]					1.0	7.20[a]	5.31[a]	7.26[a]	5.92

the bilayer, the only noteworthy change is in the amplitudes of the spectral features, whereas for the monolayer the differences in the energies of the spectral features ($\sim$ 0.1 eV) is somewhat more noticeable. Thus, use of non-optimal parameters, (α^*, γ^*), for the bilayer will overestimate exciton binding energies by $\sim$ 0.5 eV. Mitigating these errors may require a more complex multi-objective error function or the development of alternative dielectric screening models that explicitly account for the thickness of the 2D layer/slab [145]–[147].

3.1.8 h-BN

The tuned SRSH parameters, (α^*, γ^*), for bulk and monolayer h-BN were reported in Ref. [56] and are listed in Table 4. Following the same tuning procedure, we first perform GW calculations to determine the reference quasiparticle band gaps for h-BN bilayers (see SM and Table 4). Figure 31(a) exhibit ΔE_g contour plots for monolayer, bilayer, and bulk h-BN. Also in this case, the optimal parameters for the bilayer and bulk, labeled α' and γ', are not identical to those optimized for the monolayer and bulk (α^*, γ^*), differing mostly in the range-separation parameter γ. The SRSH bandstructure for the bilayer is displayed in Figure 31(b), along with the reference GW calculation. Here the extrapolation difference is 160 meV. The two results are in good agreement. Considering the lowermost conduction band and the uppermost valence band, the mean absolute error is 0.207 eV. The TD-SRSH spectrum for the bilayer is displayed in Figure 31(c), along with the reference GW-BSE spectrum. Clearly, the former is blue-shifted by approximately 0.6 eV relative to latter. This is a known issue, discussed previously in Ref. [56] and is not pursued further here.

Finally, in Figure 32 we assess the transferability of the parameters (α^*, γ^*) and (α', γ') between monolayer, bilayer, and bulk h-BN, as done in Figure 30 for MoS_2. For bulk h-BN, the bandstructure and optical spectrum is insensitive to the choice of parameters. For the monolayer and bilayer, in contrast, using the non-optimal set of parameters leads to nearly rigid shifts of the bandstructure by $\sim$ 0.35 eV. We also display in Figure 32 the TD-SRSH absorption spectra for the monolayer and bilayer using the two different sets of parameters for α and γ. Noting that the absorption spectrum suffers from a large blue-shift, as discussed above, we only seek to understand *relative* differences between the TD-SRSH spectra. For both monolayer and bilayer h-BN, the position of the first excitonic peak changes only slightly by about 0.03 eV and the peak heights are also only slightly affected. The exciton-binding energy, however, does not change by the same

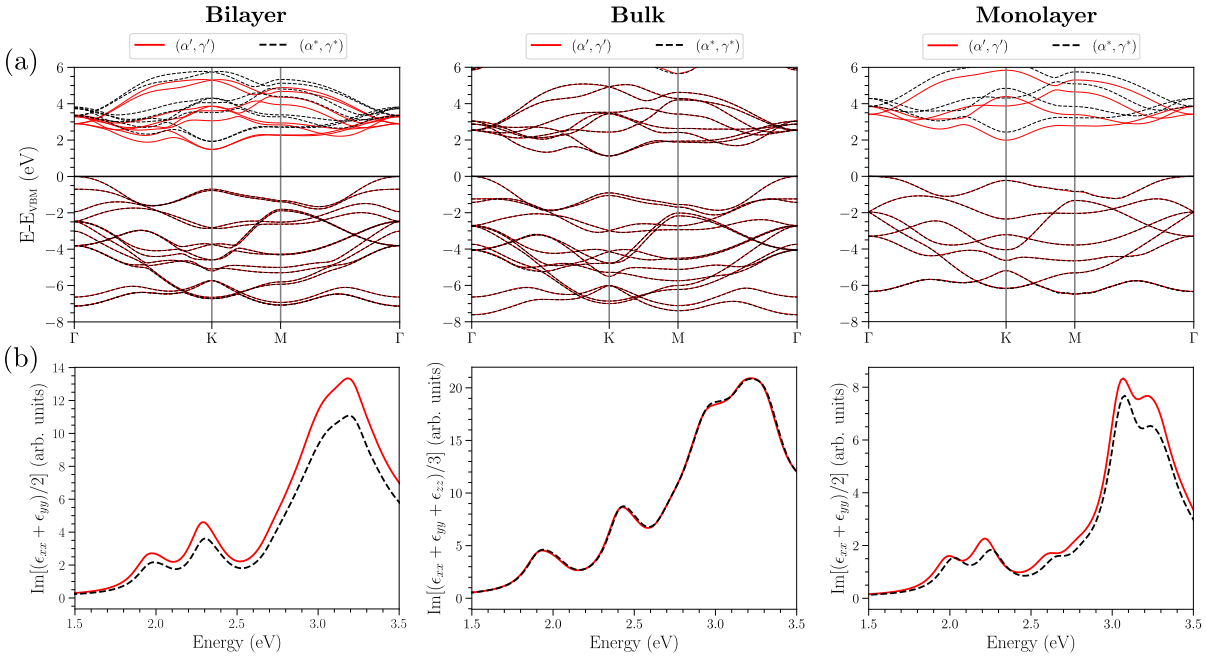

Figure 30: (a) Band structures of MoS_2 in the bilayer, bulk and monolayer phases, calculated using the parameters indicated in Table 4 and with $(\alpha^*, \gamma^*) = (0.107, 0.038\,\text{Å}^{-1})$ and $(\alpha', \gamma') = (0.105, 0.008\,\text{Å}^{-1})$, obtained from the intersections between zero crossings indicated in Figure 29. The former pair is optimal for the monolayer and the latter for the bilayer. The choice of optimal versus non-optimal parameters leads to a near constant error of ~ 0.5 eV in band gaps along the indicated high-symmetry **k**-path for bilayer and monolayer. The band structure of the bulk is not sensitive to the choice of optimal parameters. (b) Optical absorption spectra for the phases and band structures in (a).

amount. This may be attributed to the approximation of $\epsilon_\infty = 1.0$ for the bilayer, showing a limitation of this approximation in the case of the bilayer phases. Beyond the first peak though, the absorption spectra show more significant changes with the appearance of additional satellite peaks and/or shoulders. It is therefore likely that the comparison between GW-BSE and TD-SRSH for h-BN (and possibly other large-gap layered insulators) needs to be revisited, an issue we will take up elsewhere.

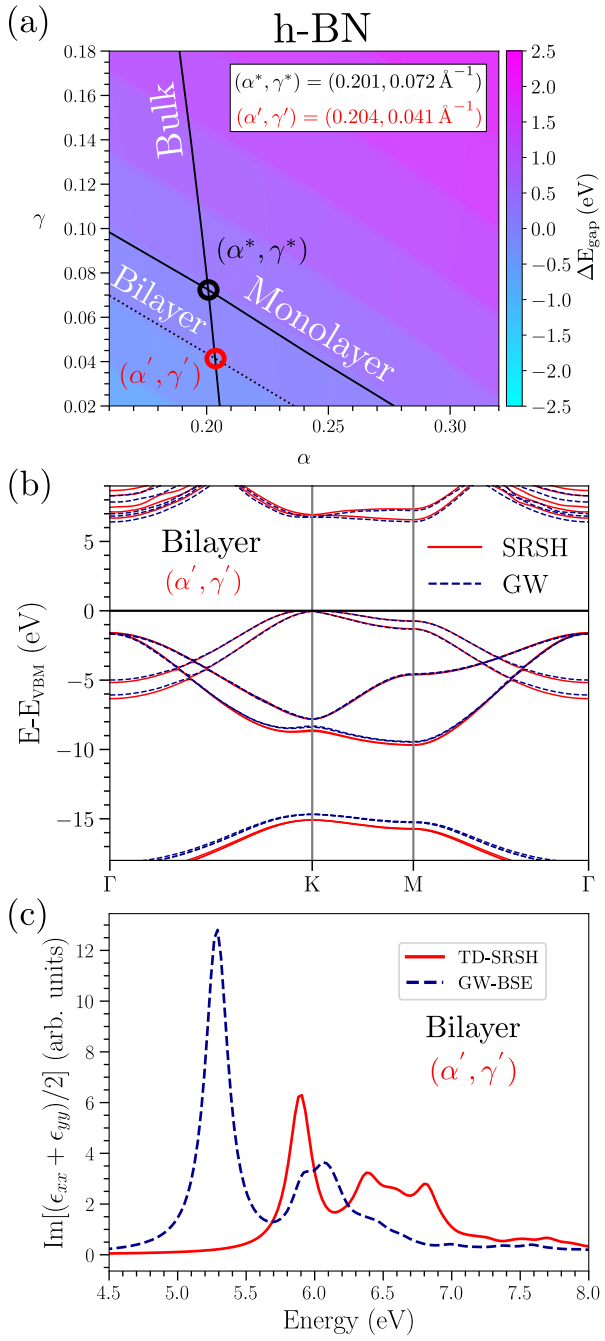

Figure 31: (a) 2D contour plots of the gap deviation, ΔE_g, for monolayer, bilayer, and bulk h-BN. The solid black lines represent the values for which $\Delta E_g = 0$ for these structures. The intersections of the solid lines yield a set of values (α^*, γ^*) that are transferable between the monolayer and bulk, and another set of values (α', γ') that are transferable between the bilayer and bulk. (b) Bandstructures for bilayer h-BN from SRSH (solid lines) using parameters (α', γ') and G_0W_0@PBE (dashed lines). (c) Optical absorption spectra for bilayer h-BN obtained with TD-SRSH (solid line) and GW-BSE (dashed line). γ has units of Å^{-1}.

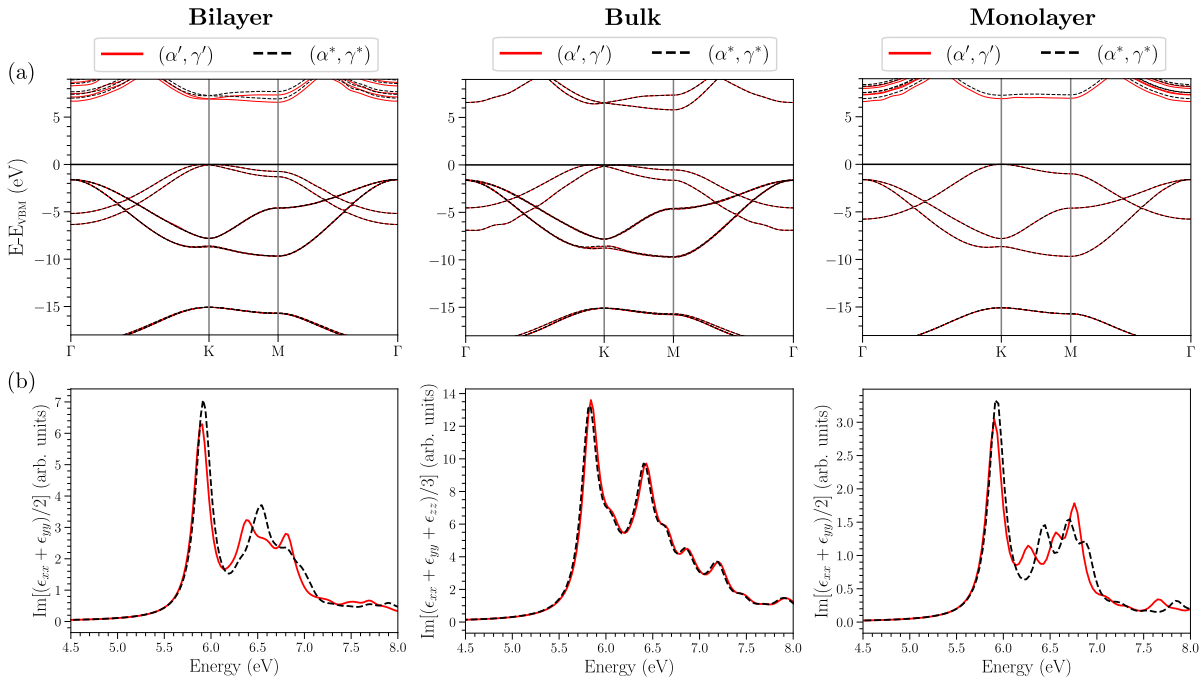

Figure 32: (a) Band structures of h-BN in the bilayer, bulk and monolayer phases, calculated using the parameters indicated in Table 4 and with $(\alpha^*, \gamma^*) = (0.201, 0.072\,\text{Å}^{-1})$ and $(\alpha', \gamma') = (0.204, 0.041\,\text{Å}^{-1})$, obtained from the intersections between zero crossings indicated in Figure 29. The former pair is optimal for the monolayer and the latter for the bilayer. The choice of optimal versus non-optimal parameters leads to a near constant error of ~ 0.35 eV in band gaps along the indicated high-symmetry **k**-path for bilayer and monolayer. The band structure of the bulk is not sensitive to the choice of optimal parameters. (b) Optical absorption spectra for the phases and band structures in (a).

3.1.9 Comparison with existing literature for semiconducting van der Waals materials

Table 3: GW band gap (E^{GW}), SRSH band gap (E^{SRSH}, fitted to an extrapolated GW quasiparticle band gap) and theoretical quasiparticle bandgap obtained from the literature ($E^{\mathrm{lit.}}$) for the materials studied in the main text. Numbers within parentheses correspond to a calculation with spin-orbit coupling. *For reference values of monolayer and bulk MoS_2, as well as h-BN, we refer the reader to Ref. [56] and references therein. [a]Ref. [148], [d]Ref. [133], both are values from GW_0. [b]Ref. [149], [c]Refs. [150], [151], [e]Ref. [125], [g]Ref. [135], [h]Ref. [152], [i]Ref. [153], are all values from G_0W_0. [f]Ref. [136], experimental value.

Material	Phase	E^{GW} [eV]	E^{SRSH} [eV]	$E^{\mathrm{lit.}}$ [eV]
WS_2	Bulk	2.32	2.29	(2.13)[a]
	1L	2.70	2.66 (2.39)	2.81[b] (2.53[c])
WSe_2	Bulk	1.97	1.94	(1.75)[a]
	1L	2.34	2.28 (1.97)	2.37[b] (2.10[c])
$MoSe_2$	Bulk	1.76	1.74	(1.83)[a]
	1L	2.06	2.04 (1.91)	2.07[b] (2.12[c])
BP	Bulk	0.49	0.56	0.58[d], 0.3[e]
	1L	1.89	1.95	2.00[e] (2.03[c])
InSe	Bulk	1.15	1.21	1.28[f]
	1L	2.90	2.87	2.87[g]
MoS_2	2L*	2.20	2.18 (2.12)	(2.30)[h]
h-BN	2L*	6.79	6.95	6.90[i]

Table 4: GW-BSE optical gap ($E_{\mathrm{opt}}^{\mathrm{GW\text{-}BSE}}$), TD-SRSH optical gap ($E_{\mathrm{opt}}^{\mathrm{TD\text{-}SRSH}}$) and experimental or theoretical optical bandgap obtained from the literature ($E_{\mathrm{opt}}^{\mathrm{lit.}}$) for the materials studied in the main text. Numbers in parentheses correspond to the position of the first absorption peak upon inclusion of spin-orbit coupling. *For reference values of monolayer and bulk MoS_2, as well as h-BN, we refer the reader to Ref. [56] and references therein. [b]Ref.[150], [151], values from GW-BSE. [i]Ref. [153], value from GW-BSE. [a]Ref. [117], experimental value. [c]Ref. [118], experimental value. [d]Ref.[119], experimental value. [e]Ref. [125], value from GW-BSE. [f]Ref. [135], experimental value. [g]Ref. [143], value from GW-BSE. [i]Ref. [144], value from GW-BSE. [j]Ref. [152], value from GW-BSE. [k]Ref. [153], value from GW-BSE.

Material	Phase	$E_{\mathrm{opt}}^{\mathrm{GW\text{-}BSE}}$ [eV]	$E_{\mathrm{opt}}^{\mathrm{TD\text{-}SRSH}}$ [eV]	$E_{\mathrm{opt}}^{\mathrm{lit.}}$ [eV]
WS_2	Bulk	2.22	2.21	-
	1L	2.29	2.32 (2.05)	2.12[a] (2.07[b])
WSe_2	Bulk	1.91	1.89	-
	1L	1.98	1.99 (1.70)	1.74[c] (1.71[b])
$MoSe_2$	Bulk	1.70	1.74	-
	1L	1.72	1.78 (1.63)	1.64[d] (1.62[b])
BP	Bulk	0.40	0.32	0.25[e]
	1L	1.34	1.38	1.2[e] (1.45[b])
InSe	Bulk	1.05	1.10	1.25[f], 1.3[g] (1.3[g])
	1L	2.67	2.76 (2.6)	2.92[f]; 2.72[g] (2.57[g])
MoS_2	2L*	1.90	1.97 (1.88)	1.91[i]; (1.9[j])
h-BN	2L*	5.29	5.91	5.3[k]

3.1.10 Application to a semi-metallic system: graphite-graphene

We provide the results that we have obtained for the most celebrated carbon allotrope in the realm of the vdW two-dimensional materials: graphene [35], and its counterpart in its bulk form, grahite, with the SRSH functionals as detailed in Sec. 2.2.

Graphene and graphite are gapless materials and this *per se* poses a challenge. In the case of graphene (monolayer phase), therefore, in order to obtain our surfaces we fit α and γ to a direct gap far from the Dirac point (the K point), for example at the Γ point. We will use the results obtained from such fitting also for graphite (bulk phase). The crystallographic structure employed in the calculations has been obtained from Ref. [154]. As for the G_0W_0 calculations, we estimate a direct band gap at the Γ point of 7.73 eV, using a k-grid of 21x21x3 for the bulk (graphite), and 7.14 eV for the monolayer with a k-grid of 24x24x1. However, in order to get an accurate band structure, avoiding the artificial gap opened due to the presence of the short range exact exchange α, we have used k-grids of 30x30x1 and 36x36x1 to obtain the band structure of graphene. In Fig. 33 we show the surfaces obtained as a result of the calculations on the left part and the projection over the $\alpha - \gamma$ space. All the calculations of the surfaces were done using the PBE functional and the PAW pseudopotentials. $(\alpha^*, \gamma^*) = (0.06, 0.03$ Å$^{-1})$ is obtained from the crossing of the bulk and the monolayer phases zero-error lines. The corresponding benchmark of the SRSH and the G_0W_0 benchmark band structures, obtained from the analysis of the surfaces and the crossings, are shown in Figure 33.

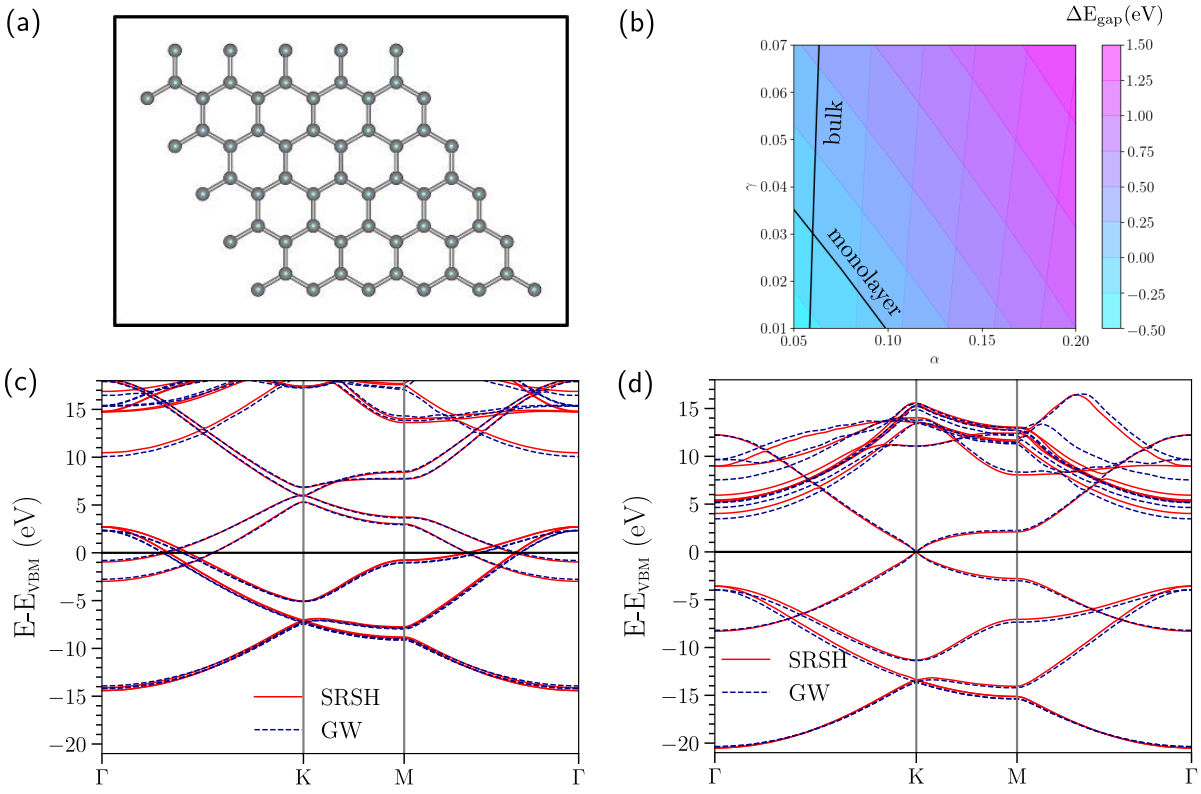

Figure 33: (a) Graphene sheet. (b) Two-dimensional projection of monolayer and bulk surfaces. The crossing between the two lines provides the point $(\alpha^*, \gamma^*) = (0.06, 0.03$ Å$^{-1})$. We use these values to obtain the band structure for graphite and graphene. (c) Bandstructure of graphite obtained with G_0W_0 and the SRSH functional. (d) Bandstructure of graphene obtained with G_0W_0 and the SRSH functional.

3.2 Nonempirical approach: Wannier-localization–based optimal tuning of a screened range-separated hybrid functional

When employing the WOT-SRSH method for small band gap materials like MoS_2 or black phosphorus, the accuracy and consistency of results compared to the semi-empirical approach discussed in Section (3.1)) are noteworthy, both for the bandstructure and optical spectra, which show only minimal deviations. The (α^*, γ^*) pairs obtained with WOT-SRSH for MoS_2 and BP are (0.126, 0.30Å^{-1}) and (0.152, 0.27Å^{-1}), respectively. Figures 34 and 36 display our results achieved with the current (WOT-)SRSH functional and compared to current state-of-the-art many-body GW-BSE methods. Notably, Figure 34 demonstrates exceptional results even without spin-orbit coupling. Moreover, Figure 35 illustrates the excellent performance of the fully non-empirical approach (WOT-SRSH) over the semi-empirical approach (OT-SRSH), with peak position deviations below 100 meV, when SOC is considered. This result are consistent with Ref. [56].

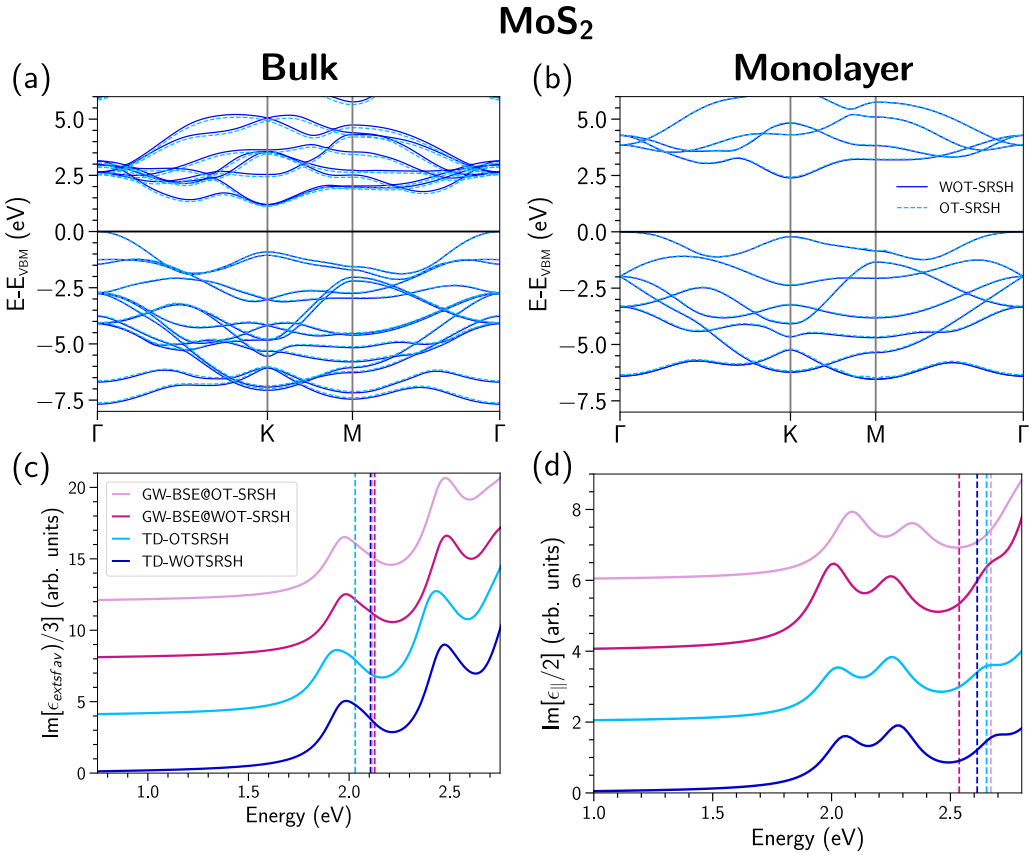

Figure 34: (a), (b) Band structure of MoS_2 bulk and monolayer without SOC. (c), (d) optical absorption spectra for black phosphorus bulk and monolayer with GW and DFT based on (W)OT-SRSH. The dashed vertical lines represent the fundamental band gap.

In Figure 37, we examine the results for h-BN using the SRSH and the WOT-SRSH approaches. With the latter method we get an $(\alpha^*, \gamma^*) = (0.343, 0.101\text{Å}^{-1})$. Additionally, a comparison with GW-BSE calculations on top of WOT- and OT-SRSH eigenenergies and eigenstates demonstrates very good agreement between the different methods. A key observation here lies in the fact that the DFT-calculated peak position has to be shifted by the zero-point renormalization (ZPR), as previously done in Ref. [29]. This aspect proves particularly critical for h-BN, a material in which the phonon contributions play a crucial role. Panels (a) and (b) in Figure 37 illustrate the outcomes without ZPR, while

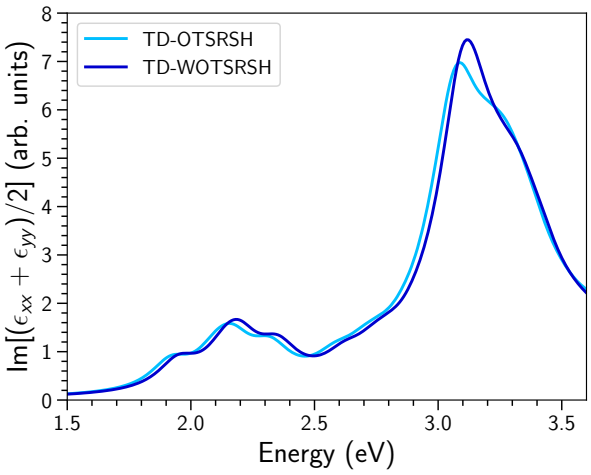

Figure 35: Optical absorption spectra of monolayer Mo_2 with SOC using the OT-SRSH (semi-empirical approach) and the WOT-SRSH functional (fully non-empirical approach).

panels (c) and (d) highlight the effects post inclusion of ZPR (383 meV at the K point for monolayer and 262 meV at the K point for the bulk h-BN, both qunatities consistent with previous results [155]). Comparison with literature values (theoretical scGW calculations and experimental data also shown in Figure 37) points towards the excellent agreement as well for GW-BSE@WOT-SRSH and TD-WOTSRSH.

Based on the results presented in this section, we draw the following conclusions: the fully non-empirical approach shows an accuracy and precision comparable to the semi-empirical technique (OT-SRSH) and can rival with the state-of-the-art methodologies, such as GW-BSE using (W)OT-SRSH. Additionally, our observations indicate that WOT-SRSH serves as a highly effective starting point for GW calculations and subsequent BSE analyses across diverse scenarios. Furthermore, the successful characterization of large-band gap materials, exemplified by h-BN, which has proved to be challenging for DFT computations, points towards the robust capability of the WOT-SRSH method. Specifically, using WOT-SRSH in the case of h-BN we have obtained consistent results compared to literature, particularly by incorporating ZPR, reinforcing its reliability and predictive capacity. This success indicates the potential for predicting electronic and optical properties for materials spanning small, medium, and large band gaps.

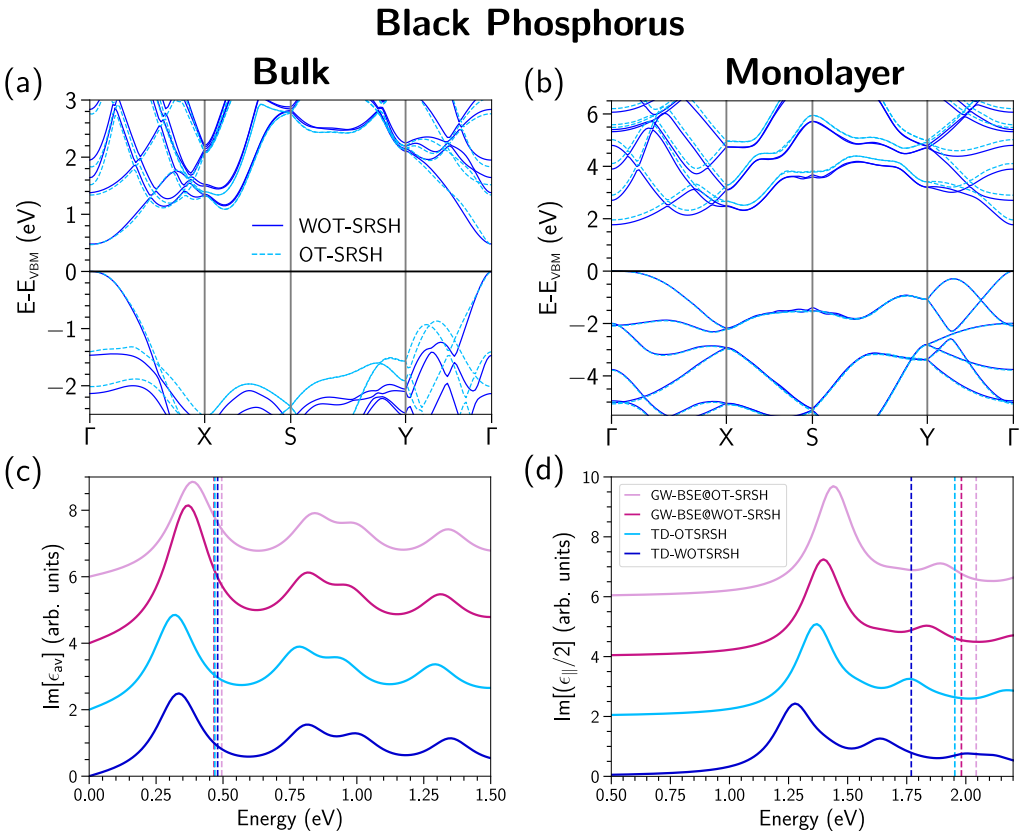

Figure 36: (a), (b) Band structure obtained with (W)OT-SRSH and (c), (d) optical absorption spectra for black phosphorus bulk and monolayer with GW and DFT based on (W)OT-SRSH. The dashed vertical lines represent the fundamental band gap.

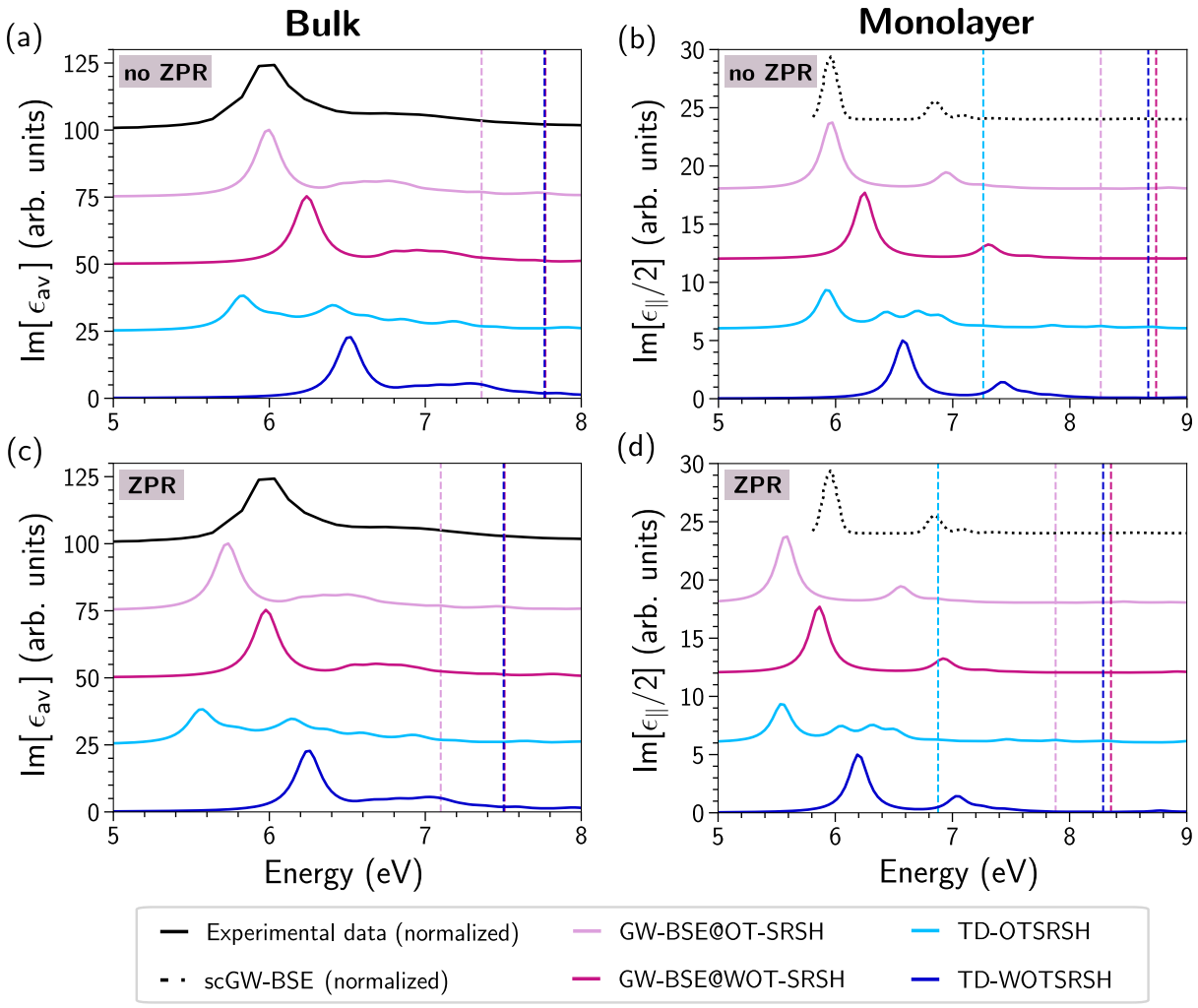

Figure 37: Optical absorption spectra of h-BN of bulk and monolayer phases w/o ZPR compared against experimental data from Ref. [156] for bulk and scGW-BSE data from Ref. [157] for the monolayer. The dashed vertical lines represente the fundamental band gap.

4 Conclusions

In conclusion, we have demonstrated a facile approach for the construction of transferable SRSH functionals for bulk and mono-/bilayer vdW materials. By tuning the SRSH functional to reproduce just one (GW) quasiparticle energy, we have demonstrated the ability to achieve excellent agreement between SRSH and GW bandstructures of bulk and mono-/bilayers TMDCs, black phosphorus, InSe, and h-BN, at a fraction of the computational cost of GW calculations. We have also shown that TD-SRSH calculations of excited-state properties, which do not enter at any stage into the functional tuning procedure, are generally in good agreement with the BSE approach, thus lending credence to the predictive capability of the SRSH/TD-SRSH formalism. The one exception to this finding is h-BN, the optical spectra of which are at variance with their BSE counterparts. As no such deviations have been reported before for SRSH studies of bulk insulators [26], it remains to be understood if this is a generic problem posed by large-gap 2D insulators which manifests in all phases of such materials and, if so, how to incorporate missing physical effects into the SRSH exchange-correlation kernel. Furthermore, more research must be carried out in the case of few-layered materials, where the approximation $\epsilon_\infty = 1.0$ may present limitations in capturing some physical properties quantitatively.

One difficulty arises if the exciton binding energy is very small. The expected level of agreement between GW and SRSH, and also between GW-BSE and TD-SRSH, is of the order of 0.1 – 0.15 eV. This is usually within the experimental accuracy of the measurements and also results in errors much smaller than the value itself, either for the band gap energy and the optical gap. An error of 0.1 eV, which is an excellent outcome in itself, can still lead to a 50% error in the exciton binding energy. For the case of small band gap materials, for example BP, the error may be even bigger. Therefore, interpretation of exciton binding energies should be performed with caution.

Also we conclude that the fully non-empirical approach demonstrates an accuracy and precision on par with the semi-empirical technique (OT-SRSH) and can compete with state-of-the-art methodologies, such as GW-BSE using (W)OT-SRSH. Our findings also suggest that WOT-SRSH serves as an exceptionally effective starting point for GW calculations and subsequent BSE analyses in diverse scenarios. Notably, the successful characterization of large-band gap materials, exemplified by h-BN—traditionally challenging for DFT computations—underscores the robust capability of the WOT-SRSH method. Specifically, employing WOT-SRSH in the case of h-BN has yielded consistent results compared to the existing literature, especially with the incorporation of ZPR, thereby reinforcing its reliability and predictive capacity. This achievement underscores the method's potential for predicting electronic and optical properties across materials with small, medium, and large band gaps.

Our results suggest that the SRSH/TD-SRSH approach is robust for 2D semiconductors, opening up a range of opportunities for accurate calculations of the optoelectronic properties of layered materials with defects, hetero-layers/-junctions, twisted or shifted layers, and more.

References

[1] R. M. Martin, "Electronic Structure: Basic Theory and Practical Methods," in Cambridge University Press, 2008.

[2] G. Onida, L. Reining, and A. Rubio, "Electronic excitations: density-functional versus many-body Green's-function approaches," *Rev. Mod. Phys.*, vol. 74, pp. 601–659, 2002.

[3] R. M. Martin, L. Reining, and D. M. Ceperley, "Interacting Electrons: Theory and Computational Approaches," in Cambridge University Press, 2016.

[4] D. Golze, M. Dvorak, and P. Rinke, "The GW Compendium: A Practical Guide to Theoretical Photoemission Spectroscopy," *Front. Chem.*, vol. 7, p. 377, 2019.

[5] M. Dreizler and E. K. U. Gross, "Density Functional Theory: An Approach to the Quantum Many-Body Problem," in Springer, Berlin, 1990.

[6] R. G. Parr and W. Yang, "Density Functional Theory of Atoms and Molecules," in Oxford University Press, Oxford, 1989.

[7] M. J. van Setten, F. Caruso, S. Sharifzadeh, *et al.*, "GW100: Benchmarking G_0W_0 for Molecular Systems," *J. Chem. Theory Comput.*, vol. 11, no. 12, pp. 5665–5687, 2015.

[8] P. Rinke, A. Qteish, J. Neugebauer, C. Freysoldt, and M. Scheffler, "Combining GW calculations with exact-exchange density-functional theory: an analysis of valence-band photoemission for compound semiconductors," *New J. Phys.*, vol. 7, pp. 126–126, 2005.

[9] J. Lischner, S. Sharifzadeh, J. Deslippe, J. B. Neaton, and S. G. Louie, "Effects of self-consistency and plasmon-pole models on GW calculations for closed-shell molecule," *Phys. Rev. B*, vol. 90, p. 115 130, 2014.

[10] C. A. Ullrich, *Time-Dependent Density-Functional Theory: Concepts and Applications*. Oxford University Press, 2011.

[11] M. A. L. Marques, N. T. Maitra, F. M. S. Nogueira, E. K. U. Gross, and A. Rubio, *Fundamentals of Time-dependent density-functional theory*. Springer, Heidelberg, 2012.

[12] L. Kronik and J. B. Neaton, "Excited-State Properties of Molecular Solids from First Principles," *Annu. Rev. Phys. Chem.*, vol. 67, no. 1, pp. 587–616, 2016.

[13] L. Kronik and S. Kümmel, "Dielectric Screening Meets Optimally Tuned Density Functionals," *Adv. Mater.*, vol. 30, no. 41, p. 1 706 560, 2018.

[14] M. Gerosa, C. E. Bottani, L. Caramella, G. Onida, C. Di Valentin, and G. Pacchioni, "Electronic structure and phase stability of oxide semiconductors: Performance of dielectric-dependent hybrid functional dft, benchmarked against *GW* band structure calculations and experiments," *Phys. Rev. B*, vol. 91, p. 155 201, 15 2015.

[15] A. Tal, P. Liu, G. Kresse, and A. Pasquarello, "Accurate optical spectra through time-dependent density functional theory based on screening-dependent hybrid functionals," *Phys. Rev. Res.*, vol. 2, p. 032 019, 3 2020.

[16] T. Leininger, H. Stoll, H.-J. Werner, and A. Savin, "Combining long-range configuration interaction with short-range density functionals," *Chem. Phys. Lett.*, vol. 275, no. 3, pp. 151–160, 1997, ISSN: 0009-2614.

[17] T. Yanai, D. P. Tew, and N. C. Handy, "A new hybrid exchange–correlation functional using the Coulomb-attenuating method (CAM-B3LYP)," *Chem. Phys. Lett.*, vol. 393, no. 1, pp. 51–57, 2004, ISSN: 0009-2614.

[18] M. A. Rohrdanz, K. M. Martins, and J. M. Herbert, "A long-range-corrected density functional that performs well for both ground-state properties and time-dependent density functional theory excitation energies, including charge-transfer excited states," *J. Chem. Phys.*, vol. 130, no. 5, p. 054 112, 2009.

[19] J. P. Perdew, R. G. Parr, M. Levy, and J. L. Balduz, "Density-Functional Theory for Fractional Particle Number: Derivative Discontinuities of the Energy," *Phys. Rev. Lett.*, vol. 49, pp. 1691–1694, 1982.

[20] M. Levy, J. P. Perdew, and V. Sahni, "Exact differential equation for the density and ionization energy of a many-particle system," *Phys. Rev. A*, vol. 30, pp. 2745–2748, 1984.

[21] C.-O. Almbladh and U. von Barth, "Exact results for the charge and spin densities, exchange-correlation potentials, and density-functional eigenvalues," *Phys. Rev. B*, vol. 31, pp. 3231–3244, 1985.

[22] J. P. Perdew and M. Levy, "Comment on "Significance of the highest occupied Kohn-Sham eigenvalue"," *Phys. Rev. B*, vol. 56, pp. 16 021–16 028, 1997.

[23] T. Stein, H. Eisenberg, L. Kronik, and R. Baer, "Fundamental Gaps in Finite Systems from Eigenvalues of a Generalized Kohn-Sham Method," *Phys. Rev. Lett.*, vol. 105, p. 266 802, 2010.

[24] L. Kronik, T. Stein, S. Refaely-Abramson, and R. Baer, "Excitation Gaps of Finite-Sized Systems from Optimally Tuned Range-Separated Hybrid Functionals," *J. Chem. Theory Comput.*, vol. 8, no. 5, pp. 1515–1531, 2012.

[25] S. Refaely-Abramson, S. Sharifzadeh, M. Jain, R. Baer, J. B. Neaton, and L. Kronik, "Gap renormalization of molecular crystals from density-functional theory," *Phys. Rev. B*, vol. 88, p. 081 204, 2013.

[26] S. Refaely-Abramson, M. Jain, S. Sharifzadeh, J. B. Neaton, and L. Kronik, "Solid-state optical absorption from optimally tuned time-dependent range-separated hybrid density functional theory," *Phys. Rev. B*, vol. 92, p. 081 204, 2015.

[27] D. Wing, G. Ohad, J. B. Haber, *et al.*, "Band gaps of crystalline solids from Wannier-localization based optimal tuning of a screened range-separated hybrid functional," *PNAS*, vol. 118, no. 34, e2104556118, 2021.

[28] G. Ohad, D. Wing, S. E. Gant, *et al.*, "Band gaps of halide perovskites from a wannier-localized optimally tuned screened range-separated hybrid functional," *Phys. Rev. Materials*, vol. 6, p. 104 606, 10 2022.

[29] G. Ohad, S. E. Gant, D. Wing, *et al.*, "Optical absorption spectra of metal oxides from time-dependent density functional theory and many-body perturbation theory based on optimally-tuned hybrid functionals," *Phys. Rev. Mater.*, vol. 7, p. 123 803, 12 2023.

[30] D. Wing, J. B. Haber, R. Noff, *et al.*, "Comparing time-dependent density functional theory with many-body perturbation theory for semiconductors: Screened range-separated hybrids and the GW plus Bethe-Salpeter approach," *Phys. Rev. Materials*, vol. 3, p. 064 603, 6 2019.

[31] S. E. Gant, J. B. Haber, M. R. Filip, *et al.*, "Optimally tuned starting point for single-shot GW calculations of solids," *Phys. Rev. Mater.*, vol. 6, p. 053 802, 5 2022.

[32] A. K. Geim and I. V. Grigorieva, "Van der Waals heterostructures," *Nature*, vol. 499, pp. 419–425, 2013.

[33] K. S. Novoselov, A. Mishchenko, A. Carvalho, and A. H. C. Neto, "2D materials and van der Waals heterostructures," *Science*, vol. 353, no. 6298, aac9439, 2016.

[34] P. M. Ajayan, P. Kim, and K. Banerjee, "Two-dimensional van der Waals materials," *Phys. Today*, vol. 69, pp. 38–44, 2016.

[35] K. S. Novoselov, A. K. Geim, S. V. Morozov, *et al.*, "Electric field effect in atomically thin carbon films," *Science*, vol. 306, no. 5696, pp. 666–669, 2004.

[36] K. S. Novoselov, D. Jiang, F. Schedin, *et al.*, "Two-dimensional atomic crystals," *PNAS*, vol. 102, no. 30, pp. 10 451–10 453, 2005.

[37] Y. Liu, N. O. Weiss, X. Duan, H.-C. Cheng, Y. Huang, and X. Duan, "Van der waals heterostructures and devices," *Nat. Rev. Mater.*, vol. 1, no. 9, p. 16 042, 2016, ISSN: 2058-8437.

[38] L. Balents, C. R. Dean, D. K. Efetov, and A. F. Young, "Superconductivity and strong correlations in moiré flat bands," *Nat. Phys.*, vol. 16, no. 7, pp. 725–733, 2020, ISSN: 1745-2481.

[39] E. Y. Andrei, D. K. Efetov, P. Jarillo-Herrero, *et al.*, "The marvels of Moiré materials," *Nat. Rev. Mater.*, vol. 6, no. 3, pp. 201–206, 2021, ISSN: 2058-8437.

[40] F. He, Y. Zhou, Z. Ye, *et al.*, "Moiré patterns in 2D materials: A review," *ACS Nano*, vol. 15, no. 4, pp. 5944–5958, 2021.

[41] M. Vizner Stern, Y. Waschitz, W. Cao, *et al.*, "Interfacial ferroelectricity by van der Waals sliding," *Science*, vol. 372, pp. 1462–1466, 2021.

[42] S. Deb, W. Cao, N. Raab, *et al.*, "Cumulative polarization in conductive interfacial ferroelectrics," *Nature*, vol. 612, pp. 465–469, 2022.

[43] A. Castellanos-Gomez, X. Duan, Z. Fei, *et al.*, "Van der waals heterostructures," *Nat. Rev. Methods Primers*, vol. 2, no. 1, p. 58, 2022, ISSN: 2662-8449.

[44] L. Hedin, "New method for calculating the one-particle green's function with application to the electron-gas problem," *Phys. Rev.*, vol. 139, A796–A823, 3A 1965.

[45] M. S. Hybertsen and S. G. Louie, "Electron correlation in semiconductors and insulators: Band gaps and quasiparticle energies," *Phys. Rev. B*, vol. 34, pp. 5390–5413, 1986.

[46] M. Rohlfing and S. G. Louie, "Electron-hole excitations in semiconductors and insulators," *Phys. Rev. Lett.*, vol. 81, pp. 2312–2315, 11 1998.

[47] S. Albrecht, L. Reining, R. Del Sole, and G. Onida, "Ab initio calculation of excitonic effects in the optical spectra of semiconductors," *Phys. Rev. Lett.*, vol. 80, pp. 4510–4513, 20 1998.

[48] D. Y. Qiu, F. H. da Jornada, and S. G. Louie, "Optical spectrum of MoS_2: Many-body effects and diversity of exciton states," *Phys. Rev. Lett.*, vol. 111, p. 216 805, 21 2013.

[49] D. Y. Qiu, F. H. da Jornada, and S. G. Louie, "Erratum: Optical spectrum of MoS_2: Many-body effects and diversity of exciton states [phys. rev. lett. 111, 216805 (2013)]," *Phys. Rev. Lett.*, vol. 115, p. 119 901, 11 2015.

[50] J. Liu, Z. Li, X. Zhang, and G. Lu, "Unraveling energy and charge transfer in type-ii van der waals heterostructures," *npj Comput. Mater.*, vol. 7, no. 1, p. 191, 2021, ISSN: 2057-3960.

[51] M. Bernardi, C. Ataca, M. Palummo, and J. C. Grossman, "Optical and electronic properties of two-dimensional layered materials," *Nanophotonics*, vol. 6, no. 2, pp. 479–493, 2017.

[52] C. Attaccalite, M. S. Prete, M. Palummo, and O. Pulci, "Interlayer and intralayer excitons in AlN/WS_2 heterostructure," *Materials*, vol. 15, no. 23, p. 8318, 2022, ISSN: 1996-1944.

[53] L. Xu, M. Yang, S. J. Wang, and Y. P. Feng, "Electronic and optical properties of the monolayer group-iv monochalcogenides MX ($M = \mathrm{Ge},\ \mathrm{Sn}$; $X = \mathrm{S},\ \mathrm{Se},\ \mathrm{Te}$)," *Phys. Rev. B*, vol. 95, p. 235 434, 23 2017.

[54] M. Govoni and G. Galli, "Large scale GW calculations," *J. Chem. Theory Comput.*, vol. 11, no. 6, pp. 2680–2696, 2015, ISSN: 1549-9618.

[55] M. Del Ben, F. H. da Jornada, A. Canning, *et al.*, "Large-scale GW calculations on pre-exascale HPC systems," *Comput. Phys. Commun.*, vol. 235, pp. 187–195, 2019, ISSN: 0010-4655.

[56] A. Ramasubramaniam, D. Wing, and L. Kronik, "Transferable screened range-separated hybrids for layered materials: The cases of MoS_2 and h-BN," *Phys. Rev. Materials*, vol. 3, p. 084 007, 8 2019.

[57] P. Ghosez, X. Gonze, and R. W. Godby, "Long-wavelength behavior of the exchange-correlation kernel in the Kohn-Sham theory of periodic systems," *Phys. Rev. B*, vol. 56, pp. 12 811–12 817, 20 1997.

[58] K. Andersen, S. Latini, and K. S. Thygesen, "Dielectric genome of van der waals heterostructures," *Nano Lett.*, vol. 15, no. 7, pp. 4616–4621, 2015.

[59] D. Y. Qiu, F. H. da Jornada, and S. G. Louie, "Screening and many-body effects in two-dimensional crystals: Monolayer MoS_2," *Phys. Rev. B*, vol. 93, p. 235 435, 23 2016.

[60] A. Seidl, A. Görling, P. Vogl, J. A. Majewski, and M. Levy, "Generalized Kohn-Sham schemes and the band-gap problem," *Phys. Rev. B*, vol. 53, pp. 3764–3774, 7 1996.

[61] S. Kümmel and L. Kronik, "Orbital-dependent density functionals: Theory and applications," *Rev. Mod. Phys.*, vol. 80, pp. 3–60, 2008.

[62] R. Baer, E. Livshits, and U. Salzner, "Tuned Range-Separated Hybrids in Density Functional Theory," *Annu. Rev. Phys. Chem.*, vol. 61, no. 1, pp. 85–109, 2010.

[63] M. Gajdo š, K. Hummer, G. Kresse, J. Furthmüller, and F. Bechstedt, "Linear optical properties in the projector-augmented wave methodology," *Phys. Rev. B*, vol. 73, p. 045 112, 4 2006.

[64] D. Wing, J. B. Neaton, and L. Kronik, "Time-dependent density functional theory of narrow band gap semiconductors using a screened range-separated hybrid functional," *Adv. Theory Simul.*, vol. 3, no. 12, p. 2 000 220, 2020.

[65] W. Chen, S. M. Griffin, G.-M. Rignanese, and G. Hautier, "Nonunique fraction of fock exchange for defects in two-dimensional materials," *Phys. Rev. B*, vol. 106, p. L161107, 16 2022.

[66] S. Refaely-Abramson, R. Baer, and L. Kronik, "Fundamental and excitation gaps in molecules of relevance for organic photovoltaics from an optimally tuned range-separated hybrid functional," *Phys. Rev. B*, vol. 84, p. 075 144, 7 2011.

[67] J. Autschbach and M. Srebro, "Delocalization Error and "Functional Tuning" in Kohn–Sham Calculations of Molecular Properties," *Accounts of Chemical Research*, vol. 47, no. 8, pp. 2592–2602, 2014.

[68] H. Phillips, Z. Zheng, E. Geva, and B. D. Dunietz, "Orbital gap predictions for rational design of organic photovoltaic materials," *Org. Electron.*, vol. 15, no. 7, pp. 1509–1520, 2014, ISSN: 1566-1199.

[69] M. E. Foster, J. D. Azoulay, B. M. Wong, and M. D. Allendorf, "Novel metal–organic framework linkers for light harvesting applications," *Chem. Sci.*, vol. 5, pp. 2081–2090, 5 2014.

[70] T. Körzdörfer and J.-L. Brédas, "Organic electronic materials: Recent advances in the dft description of the ground and excited states using tuned range-separated hybrid functionals," *Acc. Chem. Res.*, vol. 47, no. 11, pp. 3284–3291, 2014.

[71] C. Faber, P. Boulanger, C. Attaccalite, I. Duchemin, and X. Blase, "Excited states properties of organic molecules: from density functional theory to the *GW* and Bethe-Salpeter Green's function formalisms," *Philosophical Transactions of the Royal Society A: Mathematical, Physical and Engineering Sciences*, vol. 372, no. 2011, p. 20 130 271, 2014.

[72] P. Mori-Sánchez, A. J. Cohen, and W. Yang, "Localization and delocalization errors in density functional theory and implications for band-gap prediction," *Phys. Rev. Lett.*, vol. 100, p. 146 401, 14 2008.

[73] E. Kraisler and L. Kronik, "Fundamental gaps with approximate density functionals: The derivative discontinuity revealed from ensemble considerations," *J. Chem. Phys.*, vol. 140, no. 18, 18A540, 2014.

[74] V. Vlček, H. R. Eisenberg, G. Steinle-Neumann, L. Kronik, and R. Baer, "Deviations from piecewise linearity in the solid-state limit with approximate density functionals," *J. Chem. Phys.*, vol. 142, no. 3, 034107, 2015.

[75] A. Görling, "Exchange-correlation potentials with proper discontinuities for physically meaningful kohn-sham eigenvalues and band structures," *Phys. Rev. B*, vol. 91, p. 245 120, 24 2015.

[76] V. I. Anisimov and A. V. Kozhevnikov, "Transition state method and wannier functions," *Phys. Rev. B*, vol. 72, p. 075 125, 7 2005.

[77] J. Ma and L.-W. Wang, "Using wannier functions to improve solid band gap predictions in density functional theory," *Sci. Rep.*, vol. 6, no. 1, p. 24 924, 2016, ISSN: 2045-2322.

[78] M. Weng, S. Li, J. Ma, J. Zheng, F. Pan, and L.-W. Wang, "Wannier koopman method calculations of the band gaps of alkali halides," *Appl. Phys. Lett.*, vol. 111, no. 5, p. 054 101, 2017.

[79] C. Li, X. Zheng, N. Q. Su, and W. Yang, "Localized orbital scaling correction for systematic elimination of delocalization error in density functional approximations," *Natl. Sci. Rev.*, vol. 5, no. 2, pp. 203–215, 2017, ISSN: 2095-5138.

[80] G. Miceli, W. Chen, I. Reshetnyak, and A. Pasquarello, "Nonempirical hybrid functionals for band gaps and polaronic distortions in solids," *Phys. Rev. B*, vol. 97, p. 121 112, 12 2018.

[81] N. L. Nguyen, N. Colonna, A. Ferretti, and N. Marzari, "Koopmans-compliant spectral functionals for extended systems," *Phys. Rev. X*, vol. 8, p. 021 051, 2 2018.

[82] T. Bischoff, I. Reshetnyak, and A. Pasquarello, "Adjustable potential probes for band-gap predictions of extended systems through nonempirical hybrid functionals," *Phys. Rev. B*, vol. 99, p. 201 114, 20 2019.

[83] T. Bischoff, J. Wiktor, W. Chen, and A. Pasquarello, "Nonempirical hybrid functionals for band gaps of inorganic metal-halide perovskites," *Phys. Rev. Mater.*, vol. 3, p. 123 802, 12 2019.

[84] J. D. Elliott, N. Colonna, M. Marsili, N. Marzari, and P. Umari, "Koopmans meets bethe–salpeter: Excitonic optical spectra without gw," *J. Chem. Theory Comput.*, vol. 15, no. 6, pp. 3710–3720, 2019.

[85] M. Weng, F. Pan, and L.-W. Wang, "Wannier–koopmans method calculations for transition metal oxide band gaps," *NPJ Comput. Mater.*, vol. 6, no. 1, pp. 1–8, 2020.

[86] N. Q. Su, A. Mahler, and W. Yang, "Preserving symmetry and degeneracy in the localized orbital scaling correction approach," *J. Phys. Chem. Lett.*, vol. 11, no. 4, pp. 1528–1535, 2020.

[87] T. Bischoff, I. Reshetnyak, and A. Pasquarello, "Band gaps of liquid water and hexagonal ice through advanced electronic-structure calculations," *Phys. Rev. Res.*, vol. 3, no. 2, p. 023 182, 2021.

[88] N. Colonna, R. De Gennaro, E. Linscott, and N. Marzari, "Koopmans spectral functionals in periodic boundary conditions," *J. Chem. Theory Comput.*, vol. 18, no. 9, pp. 5435–5448, 2022.

[89] A. Mahler, J. Williams, N. Q. Su, and W. Yang, "Localized orbital scaling correction for periodic systems," *Phys. Rev. B*, vol. 106, no. 3, p. 035 147, 2022.

[90] J. Yang, S. Falletta, and A. Pasquarello, "One-shot approach for enforcing piecewise linearity on hybrid functionals: Application to band gap predictions," *J. Phys. Chem. Lett.*, vol. 13, no. 13, pp. 3066–3071, 2022.

[91] R. De Gennaro, N. Colonna, E. Linscott, and N. Marzari, "Bloch's theorem in orbital-density-dependent functionals: Band structures from koopmans spectral functionals," *Phys. Rev. B*, vol. 106, no. 3, p. 035 106, 2022.

[92] E. B. Linscott, N. Colonna, R. De Gennaro, *et al.*, "Koopmans: An open-source package for accurately and efficiently predicting spectral properties with koopmans functionals," *J. Chem. Theory Comput.*, vol. 19, no. 20, pp. 7097–7111, 2023.

[93] J.-Y. Noh, H. Kim, and Y.-S. Kim, "Stability and electronic structures of native defects in single-layer MoS_2," *Phys. Rev. B*, vol. 89, p. 205 417, 20 2014.

[94] M. E. Casida, "Time-dependent density functional response theory of molecular systems: Theory, computational methods, and functionals," in *Theoretical and Computational Chemistry* (Recent Developments and Applications of Modern Density Functional Theory), Recent Developments and Applications of Modern Density Functional Theory. Elsevier, 1996, vol. 4, pp. 391–439.

[95] T. Sander, E. Maggio, and G. Kresse, "Beyond the tamm-dancoff approximation for extended systems using exact diagonalization," *Phys. Rev. B*, vol. 92, p. 045 209, 4 2015.

[96] G. Kresse and J. Furthmüller, "Efficiency of ab-initio total energy calculations for metals and semiconductors using a plane-wave basis set," *Comput. Mater. Sci.*, vol. 6, no. 1, pp. 15–50, 1996, ISSN: 0927-0256.

[97] G. Kresse and J. Furthmüller, "Efficient iterative schemes for ab initio total-energy calculations using a plane-wave basis set," *Phys. Rev. B*, vol. 54, pp. 11 169–11 186, 16 1996.

[98] P. E. Blöchl, "Projector augmented-wave method," *Phys. Rev. B*, vol. 50, pp. 17 953–17 979, 24 1994.

[99] G. Kresse and D. Joubert, "From ultrasoft pseudopotentials to the projector augmented-wave method," *Phys. Rev. B*, vol. 59, pp. 1758–1775, 3 1999.

[100] D. M. Ceperley and B. J. Alder, "Ground state of the electron gas by a stochastic method," *Phys. Rev. Lett.*, vol. 45, pp. 566–569, 7 1980.

[101] J. P. Perdew and A. Zunger, "Self-interaction correction to density-functional approximations for many-electron systems," *Phys. Rev. B*, vol. 23, pp. 5048–5079, 10 1981.

[102] J. Heyd, G. E. Scuseria, and M. Ernzerhof, "Hybrid functionals based on a screened coulomb potential," *J. Chem. Phys.*, vol. 118, pp. 8207–8215, 2003.

[103] J. Heyd, G. E. Scuseria, and M. Ernzerhof, "Erratum: "hybrid functionals based on a screened coulomb potential" [j. chem. phys. 118, 8207 (2003)]," *J. Chem. Phys.*, vol. 124, no. 21, p. 219 906, 2006.

[104] J. P. Perdew, K. Burke, and M. Ernzerhof, "Generalized gradient approximation made simple," *Phys. Rev. Lett.*, vol. 77, pp. 3865–3868, 18 1996.

[105] A. A. Mostofi, J. R. Yates, Y.-S. Lee, I. Souza, D. Vanderbilt, and N. Marzari, "Wannier90: A tool for obtaining maximally-localised Wannier functions," *Comput. Phys. Commun.*, vol. 178, no. 9, pp. 685–699, 2008, ISSN: 0010-4655.

[106] A. Tkatchenko and M. Scheffler, "Accurate molecular van der waals interactions from ground-state electron density and free-atom reference data," *Phys. Rev. Lett.*, vol. 102, p. 073 005, 7 2009.

[107] W. Schutte, J. De Boer, and F. Jellinek, "Crystal structures of tungsten disulfide and diselenide," *J. Solid State Chem.*, vol. 70, no. 2, pp. 207–209, 1987, ISSN: 0022-4596.

[108] L. M. Kulikov, A. A. Semenov-Kobzar', L. G. Aksel'rud, T. A. Lobova, and E. A. Bogachev, "Niobium, molybdenum and tungstem diselenide intercalation by copper, zinc, gallium," *Neorg. Mater.*, vol. 28, no. 3, pp. 525–530, 1992.

[109] L. Cartz, S. R. Srinivasa, R. J. Riedner, J. D. Jorgensen, and T. G. Worlton, "Effect of pressure on bonding in black phosphorus," *J. Chem. Phys.*, vol. 71, no. 4, pp. 1718–1721, 1979.

[110] K. El-Sayed, Z. K. Heiba, K. Sedeek, and H. H. Hantour, "Magnetic, electric and crystallographic properties of diluted magnetic $InSe_{(1-x)}Fe(Co)_x$ semiconductor," *Journal of Alloys and Compounds*, vol. 530, pp. 102–106, 2012, ISSN: 0925-8388.

[111] B. Schönfeld, J. J. Huang, and S. C. Moss, "Anisotropic mean-square displacements (MSD) in single-crystals of 2H- and 3R-MoS_2," *Acta. Crystallogr. B. Struct. Sci. Cryst. Eng. Mater.*, vol. 39, no. 4, pp. 404–407, 1983.

[112] A. Brager, "An x-ray examination of the structure of boron nitride," *Acta Physicochimica (USSR)*, vol. 7, pp. 699–706, 1937.

[113] R. W. G. Wyckoff, *Crystal Structures - Volume 1*, eng, 2nd ed. New York: Interscience Publishers New York, 1963.

[114] S. Refaely-Abramson, S. Sharifzadeh, N. Govind, *et al.*, "Quasiparticle Spectra from a Nonempirical Optimally Tuned Range-Separated Hybrid Density Functional," *Phys. Rev. Lett.*, vol. 109, p. 226 405, 2012.

[115] L. Kronik and S. Kümmel, "Gas-phase valence-electron photoemission spectroscopy using density functional theory," in *First Principles Approaches to Spectroscopic Properties of Complex Materials*, C. Di Valentin, S. Botti, and M. Cococcioni, Eds. Berlin, Heidelberg: Springer Berlin Heidelberg, 2014, pp. 137–191, ISBN: 978-3-642-55068-3.

[116] C. Adamo and V. Barone, "Toward reliable density functional methods without adjustable parameters: The PBE0 model," *J. Chem. Phys.*, vol. 110, no. 13, pp. 6158–6170, 1999.

[117] B. Zhu, X. Chen, and X. Cui, "Exciton binding energy of monolayer WS_2," *Sci. Rep.*, vol. 5, no. 1, p. 9218, 2015, ISSN: 2045-2322.

[118] A. T. Hanbicki, M. Currie, G. Kioseoglou, A. L. Friedman, and B. T. Jonker, "Measurement of high exciton binding energy in the monolayer transition-metal dichalcogenides WS_2 and WSe_2," *Solid State Commun.*, vol. 203, pp. 16–20, 2015, ISSN: 0038-1098.

[119] B. Han, C. Robert, E. Courtade, *et al.*, "Exciton states in monolayer $MoSe_2$ and $MoTe_2$ probed by upconversion spectroscopy," *Phys. Rev. X*, vol. 8, p. 031 073, 3 2018.

[120] C. Ferrara, E. Vigo, B. Albini, *et al.*, "Efficiency and quality issues in the production of black phosphorus by mechanochemical synthesis: A multi-technique approach," *ACS Appl. Energy Mater.*, vol. 2, no. 4, pp. 2794–2802, 2019.

[121] X. Li, J. Sun, P. Shahi, *et al.*, "Pressure-induced phase transitions and superconductivity in a black phosphorus single crystal," *PNAS*, vol. 115, no. 40, pp. 9935–9940, 2018.

[122] J. Cheng, L. Gao, T. Li, *et al.*, "Two-dimensional black phosphorus nanomaterials: Emerging advances in electrochemical energy storage science," *Nanomicro Lett.*, vol. 12, no. 1, p. 179, 2020, ISSN: 2150-5551.

[123] X. Ling, H. Wang, S. Huang, F. Xia, and M. S. Dresselhaus, "The renaissance of black phosphorus," *PNAS*, vol. 112, no. 15, pp. 4523–4530, 2015.

[124] Y. Xu, Z. Shi, X. Shi, K. Zhang, and H. Zhang, "Recent progress in black phosphorus and black-phosphorus-analogue materials: Properties, synthesis and applications," *Nanoscale*, vol. 11, no. 31, pp. 14 491–14 527, 2019, ISSN: 2040-3364.

[125] V. Tran, R. Soklaski, Y. Liang, and L. Yang, "Layer-controlled band gap and anisotropic excitons in few-layer black phosphorus," *Phys. Rev. B*, vol. 89, p. 235 319, 23 2014.

[126] T. Kotani and M. van Schilfgaarde, "All-electron GW approximation with the mixed basis expansion based on the full-potential LMTO method," *Solid State Commun.*, vol. 121, no. 9, pp. 461–465, 2002, ISSN: 0038-1098.

[127] M. van Schilfgaarde, T. Kotani, and S. V. Faleev, "Adequacy of approximations in GW theory," *Phys. Rev. B*, vol. 74, p. 245 125, 24 2006.

[128] F. Fuchs, J. Furthmüller, F. Bechstedt, M. Shishkin, and G. Kresse, "Quasiparticle band structure based on a generalized Kohn-Sham scheme," *Phys. Rev. B*, vol. 76, p. 115 109, 11 2007.

[129] J. Qiao, X. Kong, Z.-X. Hu, F. Yang, and W. Ji, "High-mobility transport anisotropy and linear dichroism in few-layer black phosphorus," *Nat. Commun.*, vol. 5, no. 1, p. 4475, 2014, ISSN: 2041-1723.

[130] W. Chen and A. Pasquarello, "Band-edge positions in GW: Effects of starting point and self-consistency," *Phys. Rev. B*, vol. 90, p. 165 133, 16 2014.

[131] L. Leppert, T. Rangel, and J. B. Neaton, "Towards predictive band gaps for halide perovskites: Lessons from one-shot and eigenvalue self-consistent GW," *Phys. Rev. Mater.*, vol. 3, p. 103 803, 10 2019.

[132] A. N. Rudenko, S. Yuan, and M. I. Katsnelson, "Toward a realistic description of multilayer black phosphorus: From *GW* approximation to large-scale tight-binding simulations," *Phys. Rev. B*, vol. 92, p. 085 419, 8 2015.

[133] V. Wang, Y. Kawazoe, and W. T. Geng, "Native point defects in few-layer phosphorene," *Phys. Rev. B*, vol. 91, p. 045 433, 4 2015.

[134] M. Dai, C. Gao, Q. Nie, *et al.*, "Properties, synthesis, and device applications of 2D layered InSe," *Adv. Mater. Technol.*, vol. 7, no. 12, p. 2 200 321, 2022, ISSN: 2365-709X.

[135] Y. Guo and J. Robertson, "Band structure, band offsets, substitutional doping, and schottky barriers of bulk and monolayer inse," *Phys. Rev. Mater.*, vol. 1, p. 044 004, 4 2017.

[136] J. F. Sánchez-Royo, G. Muñoz-Matutano, M. Brotons-Gisbert, *et al.*, "Electronic structure, optical properties, and lattice dynamics in atomically thin indium selenide flakes," *Nano Research*, vol. 7, no. 10, pp. 1556–1568, 2014, ISSN: 1998-0000.

[137] S. Lei, L. Ge, S. Najmaei, *et al.*, "Evolution of the electronic band structure and efficient photo-detection in atomic layers of InSe," *ACS Nano*, vol. 8, no. 2, pp. 1263–1272, 2014, ISSN: 1936-0851.

[138] A. Politano, D. Campi, M. Cattelan, *et al.*, "Indium selenide: An insight into electronic band structure and surface excitations," *Scientific Reports*, vol. 7, no. 1, p. 3445, 2017, ISSN: 2045-2322.

[139] D. A. Bandurin, A. V. Tyurnina, G. L. Yu, *et al.*, "High electron mobility, quantum Hall effect and anomalous optical response in atomically thin InSe," *Nat. Nanotechnol.*, vol. 12, no. 3, pp. 223–227, 2017, ISSN: 1748-3395.

[140] W. Gao, Z. Zheng, Y. Li, *et al.*, "Out of plane stacking of InSe-based heterostructures towards high performance electronic and optoelectronic devices using a graphene electrode," *J. Mater. Chem. C .*, vol. 6, no. 46, pp. 12 509–12 517, 2018, ISSN: 2050-7526.

[141] J. Jiang, J. Li, Y. Li, *et al.*, "Stable InSe transistors with high-field effect mobility for reliable nerve signal sensing," *NPJ 2D Mater. Appl.*, vol. 3, no. 1, p. 29, 2019, ISSN: 2397-7132.

[142] H. Zheng, Y. Lu, K.-H. Ye, *et al.*, "Atomically thin photoanode of InSe/graphene heterostructure," *Nat. Commun.*, vol. 12, no. 1, p. 91, 2021, ISSN: 2041-1723.

[143] M. Brotons-Gisbert, R. Proux, R. Picard, *et al.*, "Out-of-plane orientation of luminescent excitons in two-dimensional indium selenide," *Nat. Commun.*, vol. 10, no. 1, p. 3913, 2019, ISSN: 2041-1723.

[144] I. Paradisanos, S. Shree, A. George, *et al.*, "Controlling interlayer excitons in MoS_2 layers grown by chemical vapor deposition," *Nat. Commun.*, vol. 11, no. 1, p. 2391, 2020, ISSN: 2041-1723.

[145] N. Rytova, "The screened potential of a point charge in a thin film," *Mosc. Univ. Phys. Bull.*, vol. 3, p. 30, 1967.

[146] L. V. Keldysh, "Coulomb interaction in thin semiconductor and semimetal films," *JETP*, vol. 29, p. 658, 1979.

[147] M. L. Trolle, T. G. Pedersen, and V. Véniard, "Model dielectric function for 2D semiconductors including substrate screening," *Sci. Rep.*, vol. 7, no. 1, p. 39 844, 2017, ISSN: 2045-2322.

[148] H. Jiang, "Electronic band structures of molybdenum and tungsten dichalcogenides by the gw approach," *The Journal of Physical Chemistry C*, vol. 116, no. 14, pp. 7664–7671, 2012, ISSN: 1932-7447.

[149] M. Graml, K. Zollner, D. Hernangómez-Pérez, P. E. Faria Junior, and J. Wilhelm, *Low-scaling GW algorithm applied to twisted transition-metal dichalcogenide heterobilayers*, 2023.

[150] S. Haastrup, M. Strange, M. Pandey, *et al.*, "The computational 2D materials database: High-throughput modeling and discovery of atomically thin crystals," *2D Materials*, vol. 5, no. 4, p. 042 002, 2018.

[151] M. N. Gjerding, A. Taghizadeh, A. Rasmussen, *et al.*, "Recent progress of the computational 2D materials database (c2db)," *2D Materials*, vol. 8, no. 4, p. 044 002, 2021.

[152] H.-P. Komsa and A. V. Krasheninnikov, "Effects of confinement and environment on the electronic structure and exciton binding energy of mos_2 from first principles," *Phys. Rev. B*, vol. 86, p. 241 201, 24 2012.

[153] F. Paleari, T. Thomas Galvani, H. Amara, F. Ducastelle, A. Molina-Sánchez, and L. Wirtz1, "Effects of confinement and environment on the electronic structure and exciton binding energy of mos_2 from first principles," *2D Mater.*, vol. 5, p. 045 017, 2018.

[154] J. Zemann, "Crystal structures, 2nd edition. vol. 1 by R. W. G. Wyckoff," *Acta Crystallogr.*, vol. 18, no. 1, pp. 139–139, 1965.

[155] R. Tutchton, C. Marchbanks, and Z. Wu, "Structural impact on the eigenenergy renormalization for carbon and silicon allotropes and boron nitride polymorphs," *Phys. Rev. B*, vol. 97, p. 205 104, 20 2018.

[156] C. Tarrio and S. E. Schnatterly, "Interband transitions, plasmons, and dispersion in hexagonal boron nitride," *Phys. Rev. B*, vol. 40, pp. 7852–7859, 11 1989.

[157] F. Zhang, C. S. Ong, J. W. Ruan, *et al.*, "Intervalley excitonic hybridization, optical selection rules, and imperfect circular dichroism in monolayer $h-$BN," *Phys. Rev. Lett.*, vol. 128, p. 047 402, 4 2022.

List of Symbols, Abbreviations, and Acronyms

α Fraction of exact exchange
β Fractional excahnge parameter
BP Black phosphorus
BSE Bethe-Salpeter equation
DFT Density functional theory
ϵ_∞ Dielectric-screening constant
ϵ_∞ Dielectric-screening tensor
x Exchange
XX Exact exchange
γ Range-separation parameter
h-BN Hexagonal boron nitride
HSE06 Heyd–Scuseria–Ernzerhof (exchange-correlation functional)
InSe Indium selenide
IPT Ionization potential theorem
SR Long-range
MBPT Many-body perturbation theory
MoS_2 Molybdenum disulfide
$MoSe_2$ Molybdenum diselenide
(OT-)SRSH Optimally tuned screened range-separated hybrid
RPA Random phase approximation
PBE Perdew–Burke-Ernzerhof (exchange-correlation functional)
SL Semilocal
SR Short-range
SOC Spin-orbit coupling
TD-DFT Time-dependent density functional theory
TD-SRSH Time-dependent density functional theory based on screened range-separated hybrid exchange-correlation functional
TD-WOT-SRSH Time-dependent density functional theory based on Wannier-localization–based optimal tuning of screened range-separated hybrid exchange-correlation functional
vdW van der Waals
WOT-SRSH Wannier-localization–based optimal tuning of screened range-separated hybrid exchange-correlation functional
WS_2 Tungsten disulfide
WSe_2 Tungsten diselenide
ZPR Zero-point renormalization